Journal of Materials Chemistry A

Recent Theoretical Progress in Development of Photoanode Materials in Solar Water Splitting Photoelectrochemical Cells

Journal:	*Journal of Materials Chemistry A*
Manuscript ID:	TA-REV-01-2015-000257.R1
Article Type:	Review Article
Date Submitted by the Author:	10-Mar-2015
Complete List of Authors:	Bhatt, Mahesh; Ulsan National Institute of Science and Technology, Energy and Chemical Engineering Lee, Jae; Ulsan National Institute of Science and Technology, Energy and Chemical Engineering

Contents

Recent Theoretical Progress in Development of Photoanode Materials in Solar Water Splitting Photoelectrochemical Cells

Mahesh Datt Bhatt and Jae Sung Lee

School of Energy & Chemical Engineering, Ulsan National Institute of Science & Technology (UNIST), Ulsan, 689-798, Republic of Korea

Abstract

The search for earth-abundant materials that can be used in solar water splitting cells remains an important goal for affordable and environmentally benign methods for energy conversion and storage. The development of efficient photoelectrodes includes a major challenge for stability of photoelectrodes in solar water spilliting cells. This article reviews state-of-the-art theretical research activities mainly based on density functional theory (DFT) calculations in the development of efficient photoanode materials, focusing on the scientific and technological possibilities offered by photoanode materials, such as $BiVO_4$, α-Fe_2O_3, WO_3, TaON and Ta_3N_5. We start with a brief introduction to explore the suitable photoanode materials as well as to optimize their energy band configurations for specific applications. This introduction section is followed by the basic theory of photocatalysis. Finally, we discuss the current theoretical progress in the development of photoanode materials according to the DFT results available in the literatures to date. This review also highlights crucial issues that should be addressed in future research activities in summary and outlook section.

Key words: Photoanodes, water splitting, DFT, OER, HER, overpotential, charge separation.

* To whom correspondence should be addressed.
E-mail: mdbhatta2005@gmail.com

1. Introduction

The global warming, energy shortages and environmental pollution have raised awareness of a potential global crisis. Harvesting sunlight to produce clean hydrogen fuel remains one of the main challenges for solving the energy crisis and overcoming global warming [1-3]. In this sense, photoelectrochemical cell (PEC) hydrogen production is a key method for providing clean energy in the future with the use of solar energy to split water by reducing water to H_2 or reduce CO_2 to various carbon-based molecules. The anodic reaction will most likely involve the oxidation of water in both cases. The high overpotentials are required for water oxidation due to the slow kinetics involving multi-electron and multi-ptoton transfers [2, 4]. Consequently, the development of high performance and commercially viable photoelectrochemical cells with an efficient and practical anode system that can oxidize water to O_2 in a stable manner.

With this regard, many recent scientific efforts have focused on the development of n-type semiconductors that can serve as efficient photoanodes for solar water oxidation. The efficient photoanode materials should have a small band gap to utilize a significant portion of the visible light as well as enough positive valence band edge to provide sufficient overpotential for the water oxidation reaction. The position of the conduction band is also important in the sense that it determines the potential of the photo-excited electrons that can be used for cathode reaction, i.e.water or CO_2 reduction.

Density functional theory (DFT) calculations are useful theoretical tools in studying the structural and electronic properties of various photoanode materials (e.g. oxide semiconductors, oxy-nitride and nitride semiconductors). With this regard, we focus in this article on the progress of the study about five important visible light sensitive photoanode materials that demonstrate the useful activity under solar excitation in fields concerned with solar oxygen production, such as $BiVO_4$, α-Fe_2O_3, WO_3, TaON and Ta_3N_5 for PEC water oxidation

into O_2. There are already a significant number of reviews covering such subjects [5-8], but still there is scarcity for theoretical reviews based on DFT investigations for these photoanode materials. Therefore, we emphasize the important factors affecting the PEC performance of above mentioned photoanode materials and strategies of addressing the shortages of them for breaking through their limitations using computational modelings and theoretical investigations.

The recent studies on $BiVO_4$ have focused on the preparation of $BiVO_4$ as electrode-type materials for use as photoanodes for photoelectrochemical cells. However, the typical efficiencies for unmodified $BiVO_4$ photoanodes for water-oxidation were not impressive as they suffer from excessive-hole recombination, poor charge transport properties, and poor water oxidation kinetics. $BiVO_4$ is a promising photoanode material due to the fact that it is composed of inexpensive elements and has a band gap of 2.4 eV with the valence band (VB) edge located at ca. 2.4 eV vs. RHE (reversible hydrogen electrode), providing sufficient overpotential for holes to photooxidize water while the conduction band (CB) edge is located just short of the thermodynamic level for H_2 [9]. Its band gap is slightly larger than that is desired for a photoanode (ca. 2.0 eV), but it's very negative CB position may compensate for this disadvantage [10, 11].

Recently, there have been numerous theoretical studies on WO_3, including DFT and Hartree-Fock (HF) calculations [12-20]. However, most of these studies are limited to the simple-cubic system, except for three DFT studies [13, 14, 20] where the most common phases have been considered. Studies on WO_3 are mainly based on standard DFT or HF calculations [17]. Which severly underestimate or overestimate respectively, the band gap values. WO3 has attracted a lot of interest as an n-type catalyst partly due to its photosensitivity [21-23], good electron-transport properties [24], and stability against photocorossion [25, 26]. Its smaller

band gap (≈2.8 eV) [27] makes it suitable for absorption of visible solar light. However, the gap of WO_3 is still too large to realize a sufficient absorption of the solar spectrum. Moreover, experiments suggest that the conduction band minimum of bulk WO_3 is about 0.4 eV below the hydrogen redox potential [28, 29]. Therefore, a variety of dopants have been considered experimentally to improve the photocatalytic properties of WO_3.

During the last two decades, an increasing number of theoretical investigations have been performed to describe the bulk and surface properties of iron(hydr)oxides. The electronic and magnetic structure of α-Fe_2O_3 has been studied via the DFT methods [30-34], whereas similar calculations of point defects such as interstitials, vacancies and substitutional dopants in hematite have shown these to have profound effects on the electronic properties [34-37]. Computer simulations have been used successfully to investigate the interactions and properties of oxyanions on iron(hydr)oxide surfaces, predicting the stable adsorption complexes and the mechanism of sorption [38-49].

Owing to their good chemical stability in aqueous solution, transition metal oxides are the subject of most previous studies [50, 51]. However, transition metal oxides usually have large band gaps (≥ 3 eV), limiting the absorption of visible light and setting an upper limit on the energy conversion efficiency at about 2 % [50, 51]. In contrast, the transition metal nitrides have smaller band gaps due to N 2p orbitals being shallower than O 2p orbitals, but the easy oxidation of nitrides in aqueous solution makes them degraded quickly. Being in between the oxides and nitrides, the oxynitrides are believed to have intermediate properties, such as smaller band gaps than oxides and better stability than nitrides [50-52]. A well known example, tantalum oxynitride TaON, which has a band gap around 2.5 eV, between those of Ta_2O_5 (3.9 eV) and Ta_3N_5 (2.1 eV), was found to have high quantum yield for nonsacrificial visible-light-driven water splitting [53-55]. In addition, TaON has appropriate alignment of its valence and

conduction band edge relative to the OH^-/O_2 oxidation and H^+/H_2 reduction potentials, make it possible to produce H_2 and O_2 from water even without an externally applied bias [51, 55]. A few theoretical studies [56-60] have been published on the electronic structure of TaoN and Ta_3N_5.

In this theoretical review article, we discuss the recent advancement in photoanode materials based on DFT investigations. The section after a brief introduction section consists of a basic theory of photocatalysis, third section contains the recent theoretical progress in the development of photoanode materials, fourth section discusses the development of DFT methods for designing efficient photoanode materials and final section discusses the key scientific challenges that should be addressed to develop more efficient photoanodes in solar water splitting photoelectrochemical cells in summary and outlook section. We do strongly believe that such type of theoretical review may help the readers to understand the theoretical advancement of photoanode materials as well as to guide the experimentalists for further improvement of these materials in practical applications of photoelectrochemical cells.

2. Basic Theory of Photocatalysis

The schematic diagram of the basic principles of water splitting for a photoelectrochemical cell with an n-type semiconductor photoanode where O_2 evolved and a cathode where H_2 evolved, is shown in Fig. 1 [61]. The photoanode is the photoactive semiconductor material based electrode, which is irradiated by a light beam during water splitting. The cathode is not irradiated by light, so it is also known as counter electrode. The free energy change for conversion of one H_2O molecule into H_2 and 1/2 O_2 under standard conditions is ΔG = +237.2 kJ/mol, which corresponds to ΔE^0 = 1.23 V per electron transferred according to Nernst equation. In order to drive this reaction, the photoactive anode material must absorb radiant

light to make its electrode potential higher than 1.23 V. If the photoanode material is irradiated by light that has energy greater than the band gap of the photoactive material, then the electrons of the valence band (VB) will be excited into the conduction band (CB) while the holes remain in the valence band.

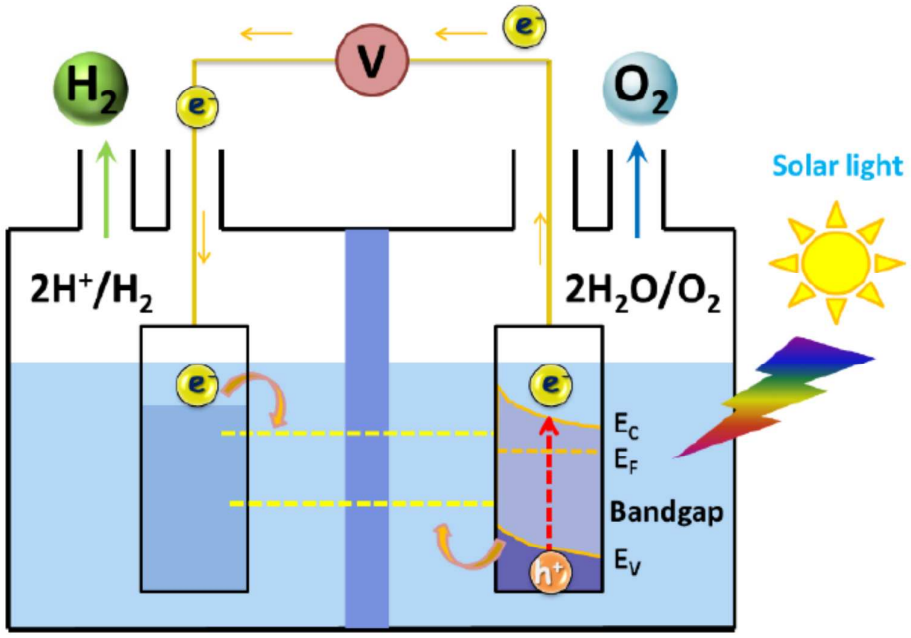

Fig. 1 Schematic diagram of the basic principles of water splitting for a photoelectrochemical cell with an n-type semiconductor photoanode where oxygen is evolved and a cathode where hydrogen is evolved [61]

Fig. 2 [10] shows the hydrogen evolution reaction (HER) and oxygen evolution reaction (OER) using electrons/holes generated under illumination:

$$H_2O + 2(h^+) \rightarrow \frac{1}{2}O_2 + 2H^+ \qquad \text{(OER; Oxidation)}$$

$$2H^+ + 2e^- \rightarrow H_2 \qquad \text{(HER; Reduction)}$$

$$H_2O \rightarrow \frac{1}{2}O_2 + H_2 \qquad (\Delta G = +237.2 \text{ kJ/mol})$$

..... (1)

To carry out one or both reactions without recombination, photo-induced electrons and holes in semiconductor must travel to liquid junction. The energy required for

photoelectrolysis at a semiconductor photoelectrode is frequently reported as 1.6-2.4 eV per electron-hole pair generated, to account for losses due to the concentration and kinetic overpotentials [62, 63]. Therefore, a photoinduced process must produce four electron-hole pairs for generating O_2 on the photoanode.

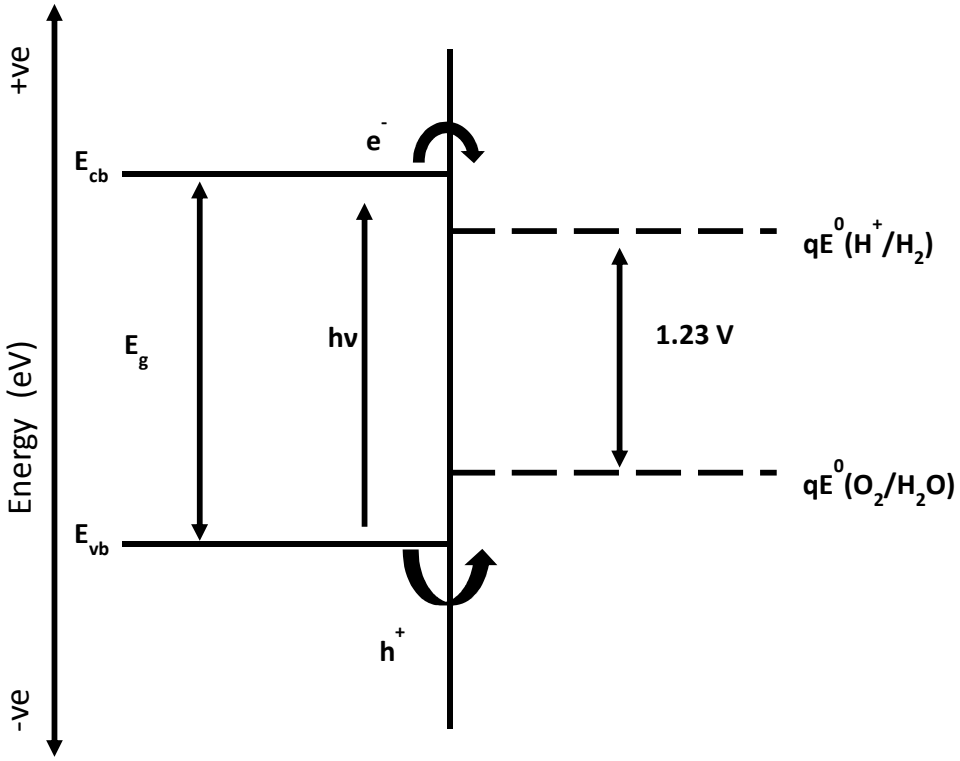

Fig. 2 Oxygen evolution reaction (OER) and hydrogen evolution reaction (HER) for overall water splitting (under acidic conditions) [10]

The incident photon-to-current conversion efficiency (IPCE) of the photoanode materials is given by

$$\text{IPCE}\ (\%) = \frac{1240J}{\lambda \times I} \times 100\% \quad \text{..... (2)}$$

Where J represents the photocurrent density (mA/cm^2), λ is the wavelength of incident light (nm), and I is the intensity of incident light (mW/cm^2).

The overall efficiency of solar energy conversion is given by

$$\eta = 100\% \times \text{J}.\,(E^0_{rex} - E)/I_{light} \quad \text{..... (3)}$$

Where E is the bias voltage applied against a counter electrode (=0 V for photoanode), J is photocurrent density (mA/cm^2) at the applied bias E, I_{light} is irradiance intensity (=100 mW/cm^2 for AM 1.5G), and E^0_{rex} is usually taken to be 1.229 V (pH = 0) for the water splitting reaction.

For the three electrode configuration of photoelectrochemical cell, the reference electrode potential vs Ag/AgCl in the reversible hydrogen electrode (RHE) scale according to the Nernst equation:

$$E_{RHE} = E_{Ag/AgCl} + 0.059pH + E^0_{Ag/AgCl} \left(E^0_{\frac{Ag}{AgCl}} = +0.199\,V \right) \quad \text{..... (4)}$$

Finally, the solar-to-hydrogen efficiency (STH) for a photoelectric system constructed by photoelectrodes with sunlight and water as inputs can be expressed as

$$\eta = 100\% \times \mathrm{J} \times 1.229/I_{light} \quad \text{..... (5)}$$

The band-edge positions vs the normal hydrogen electrode (NHE) for several common p- and n-type semiconductor materials are shown in Fig. 3 [10].

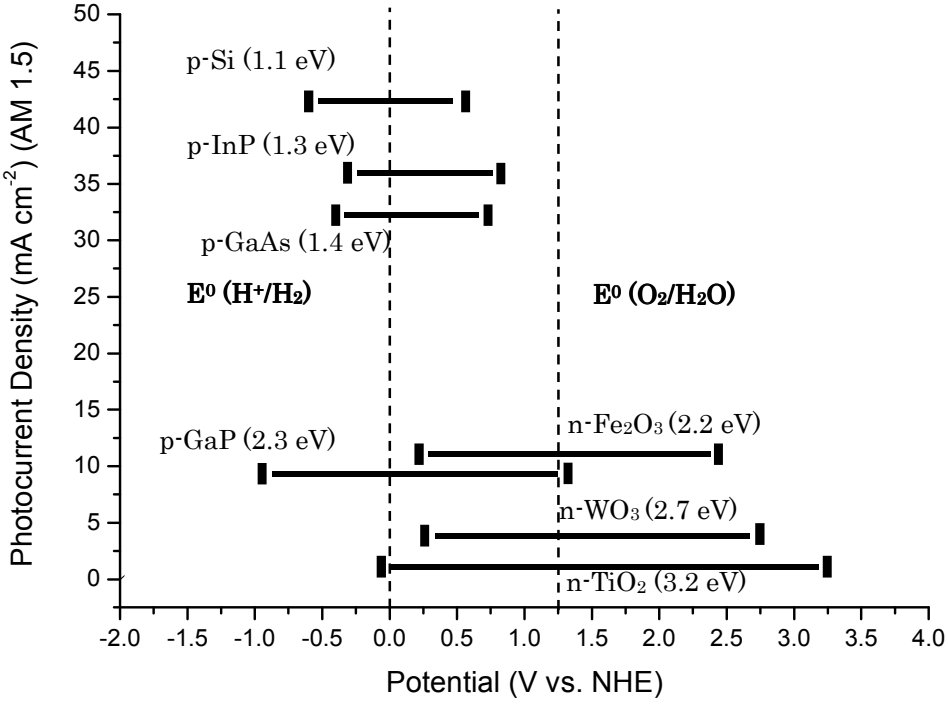

Fig. 3 Conduction band and valence band positions vs NHE of common semiconductors used

in photoelectrolysis cells. The band gap value is given in parentheses [10]

Some of the large band gap n-type semiconductors in Fig. 3 straddle the potential of the O_2/H_2O redox couple, but these materials are not capable of producing high photocurrent densities under AM 1.5 illumination. In contrast, the smaller band gap p-type materials shown in Fig. 3 [10] have more negative conduction/valence bands that are well suited to effect reactions at the H^+/H_2 potentials. It is well known that the overpotentials required to drive water oxidation and reduction are key factors for placement of the VB and CB edge positions of a semiconductor with respect to the potentials for OER and HER respectively. For an instance, water splitting can be very slow or negligible in case of a semiconductor material for which VB potential is not sufficiently positive for water oxidation or CB potential is not sufficiently negative for proton reduction. For example, in order to start to estimate the efficiency of a photoelectrode to drive the OER or HER, overpotentials of 400 mV at 10 mA/cm^2 for water oxidation and 50 mV at 10 mA/cm^2 for H_2 evolution at a semiconductor/liquid junction may be important values [64].

3. Recent Theoretical Progress in Development of Photoanode Materials

It is well known that the anodic reactions most likely involve oxidation of water, which is particularly demanding and requires high overpotentials [2, 4] due to the slow kinetics involving multi-electron and multi-proton transfers. Many recent efforts have focused on the development of n-type semiconductors that can serve as efficient photoanodes for solar water oxidation, as an important part of the successful construction of high performance and commercially viable photoelectrochemical cells. The efficient photoanodes should have a small band gap to utilize a significant portion of visible light, and a valence band edge that is positive enough to provide sufficient overpotential for the water oxidation reaction. If these electrons

don't have sufficient overpotential to reduce water, an external bias needs to be provided, effectively reducing the cell efficiency.

With this recognition, density functional theory (DFT) calculations are useful in studying the structural, electronic and optical properties of photoanode materials. Although, there have been many theoretical investigations for exploring efficient photoanode materials, it is also important to investigate stable and inexpensive photoanode materials with good charge separation and transport properties by means of theoretical modelings.

3.1 Bismuth Vanadate ($BiVO_4$)

Bismuth vanadate ($BiVO_4$) has recently emerged as a viable candidate for photocatalytic water oxidation [65-72]. $BiVO_4$ mainly exists in three different crystal phases such as tetragonal zircon (tz-), tetragonal scheelite (ts-), and monoclinic scheelite (ms-) [73]. Among these polymorphs, ms-$BiVO_4$ exhibits the highest photocatalytic activity under visible light irradiation [71, 72]. The lower activity of tz-$BiVO_4$ has been explained by the relatively large band gap (2.9 eV), while ts-BiVO4 and ms-$BiVO_4$ have similar band gaps (2.3 eV and 2.4 eV respectively [71]). The significantly enhanced photocatalytic activity of ms-$BiVO_4$ over ts-$BiVO_4$ could be some how related to the monoclinic distortion, albeit the underlying mechanism remains unclear. There have been only a few theoretical investigations for $BiVO_4$ [65, 68, 74-77]. Monoclinic clinobisvanite $BiVO_4$ with band gap about 2.4-2.5 eV has been reported to have excellent photocatalytic O_2 evolution and organic compound degradation under visible-light irradiation [66, 78-82]. It is worthy to note that $BiVO_4$ in the monoclinic clinobisvanite structure, instead of other polymorphs such as orthorhombic pucherite and tetragonal dreyerite, exhibits very high photocatalytic activity [66, 78, 81, 82]. The crystal structure of $BiVO_4$; its calculated band structure, orbital level interaction; and schematic illustration of the basic mechanism of

the $BiVO_4$-based photocatalytic process is shown in Fig. 4 [65, 95].

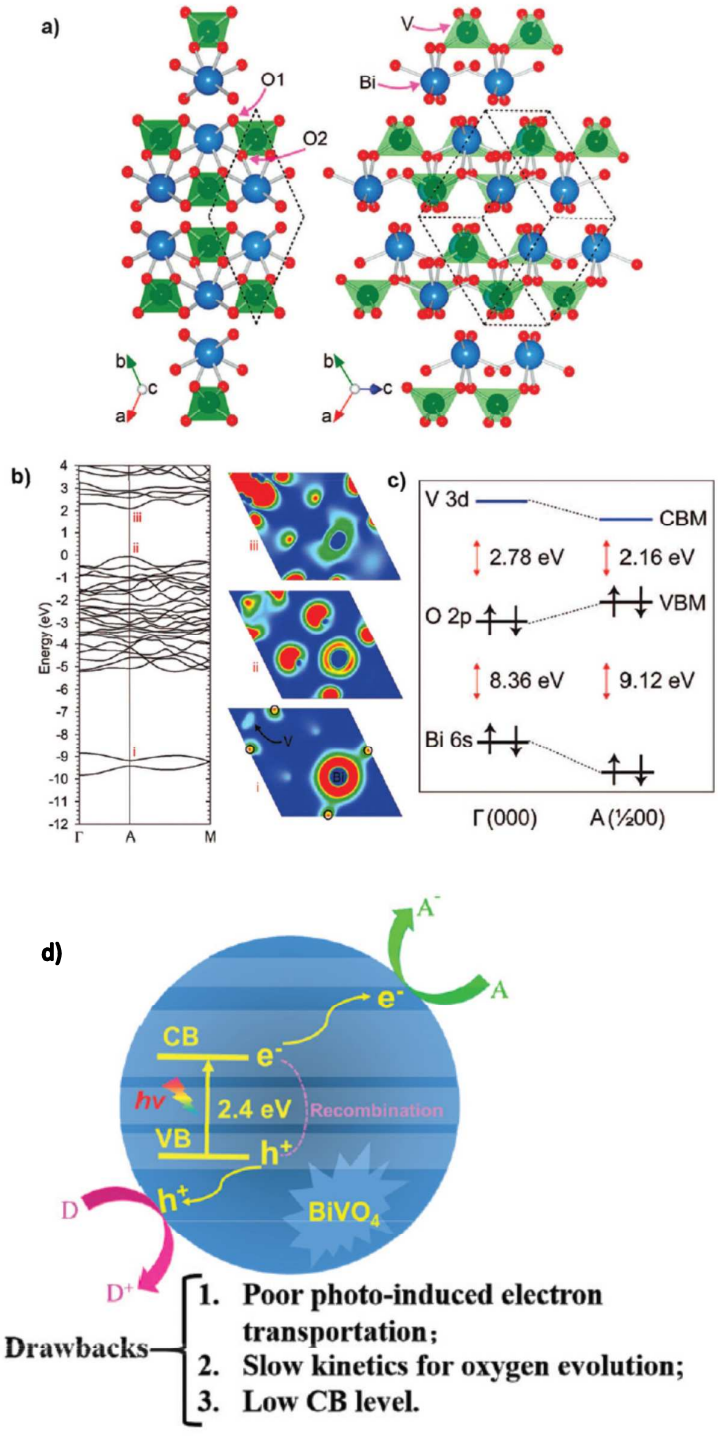

Fig. 4 (a) crystal structure of $BiVO_4$, (b) calculated band structure, (c) orbital level interaction,

and (d) schematic illustration of the basic mechanism of the $BiVO_4$-based photocatalytic process [65, 95].

By taking into account the crystal inversion symmetry, a primitive cell of two formula units can be constructed as shown in Fig. 4 (a). The Bi atom was found coordinated with a distorded oxygen octahedron with the approximate nearest neighbor distance of 2.35-2.53 Å, whereas V at the center of a distorded tetrahedron with the approximate bondlengths of 3.48 Å and 3.50 Å. O_1 was found coordinated with one Bi and V, while O_2 with two Bi and a single V. The band structure drawn along two high symmetry lines of the Brillouin zone is shown in Fig. 4 (b). The PBE-DFT band gap of $BiVO_4$ was undersimated (2.16 eV) relative to the experiment (2.4-2.5 eV) [65]. The VB and CB extrema were found away from the gamma point as these both contain contributions from O 2p and V 3d respectively; however, away from the zone center, a coupling with Bi 6s and Bi 6p/O 2p was observed [65]. The resulting energy level interactions are summarized in Fig. 4 (c). The schematic illustration of the basic mechanism of the $BiVO_4$-based photocatalytic process with drawbacks of $BiVO_4$ as a photoanode material for its lower photo-conversion efficiency is shown in Fig. 4 (d).

In 2006, Oshikiri and co-workers [83] presented first principles molecular dynamics study within the Car-Parrinello scheme (CPMD) [84], of the adsorption of H_2O molecules on the surface of $BiVO_4$. Their study revealed that a H_2O molecule is adsorbed molecularly, instead of dissociatively, at the fivefold Bi site with an adsorption energy of about 0.58 eV/molecule. In case of water adsorption at a Bi site, the distance between H_{water} and V, which is a reduction site, was found larger than in the case of adsorption at a V site, indicating that the proton reduction processes may be suppressed. In 2009, Walsh and co-workers [65] reported $BiVO_4$ to be a direct band gap semiconductor by means of first principles electronic structure calculations, despite having band extreme away from the Brillouin zone center. The coupling between Bi 6s and O 2p forced an upward dispersion of the valence band at the zero

boundaries; however, a direct gap was maintained via coupling between V 3d, O 2p, and Bi 6p, which lowers the conduction band minimum. In 2011, Park and co-workers [85] performed DFT calculations to demonstrate an increase in the photocatalytic activity of W-doped BiVO4 by additional doping with Mo. Their overall DFT results revealed that the consecutive doping of W and Mo into the metal oxide photocatalyst introduces improved electron-hole separation without a significant change of the band gap or the material's optical properties. Moreover, Zhao and co-workers [86] performed DFT calculations to study the structural, electronic, and optical properties of monoclinic clinobisvanite $BiVO_4$. Their calculated results signified that monoclinic clinobisvanite $BiVO_4$ is an indirect band gap semiconductor and there are non-bonding states both at the top of the VB and the bottom of the CB. It was also observed by the authors that there is a significant optical anisotropy near the absorption edge, which results from its special crystal structure and electronic structure. In 2012, Kweon and co-workers [87] performed hybrid density functional study of the structural, bonding, and electronic properties of monoclinic and tetragonal polymorphs of $BiVO_4$ as ms-$BiVO_4$ and ts-$BiVO_4$ using PBE and PBE-HF hybrid functionals with varying HF exchange fractions (10%, 25% and 50%). The authors found how the inclusion of exact HF exchange improves the accuracy of predicting the properties of $BiVO_4$. Their DFT results revealed that an increase in the amount of HF exchange leads to an enhancement of the antibonding interaction between Bi 6s and O 2p states as a consequence, hybridization between Bi 6s and O 2p antibonding states and unoccupied Bi 6p states becomes more pronounced to reduce the antibonding interaction through the monoclic lattice distortion, suggesting the resulting energy gain exceeding the strain energy is primarily responsible for prediction of energetically favored ms-$BiVO_4$ over ts-$BiVO_4$ when the HF exchange fraction is greater than 25%. Moreover, the authors, in 2013, have performed spin-polarized DFT calculations to investigate a possible surface effect on the

phase-dependent behavior. The authors compared the geometries and electronic structures of the monoclinic and tetragonal $BiVO_4$ (001) surfaces using hybrid density functional theory. Their DFT result indicated that the hole formation energy difference could be another factor for the phase-dependent photocatalytic activity towards water splitting due to the fact that the degrees of surface relaxation and hole localization in aqueous environments would be different from those at gas-solid interface. In 2013, Wang et al. [88] predicted by using DFT methods that both oxygen vacancies and hydrogen impurities are shallow donors for $BiVO_4$ with low formation energies, increasing the donor densities of $BiVO_4$ without introducing deep trap states. In 2014, Cooper and co-workers [89] studied the electronic structures of ms-$BiVO_4$ and ts-$BiVO_4$ to understand both the VB and CB orbital character. Their DFT results indicated that the VB maximum and CB minimum are comprised primarily of O 2p and V 3d orbitals respectively. The authors provided an additional perspective on improving the overall performance of ms-$BiVO_4$ thin films for applications in photoelectrochemical water splitting via doping or alloying. Poor electron mobility in the material was likely a consequence of the localization of V d-orbitals at the CB minimum due to poor overlap with Bi 6p-orbitals. Moreover, Ma et al. [90] performed DFT calculations to investigate the role of the isolated 6s states in $BiVO_4$. The authors found that many good properties of $BiVO_4$ for water splitting are related to the s-p coupling due to the existence of Bi 6s states. The authors also proposed the alloying Bi with Sb to improve the water splitting efficiency.

In order to improve the photoactivity, chemical treatment of $BiVO_4$ has also been investigated. For example, soaking of $BiVO_4$ films in aqueous AgNO3 solution was suggested as a material treatment to enhance its stability and photocatalytic activity for water oxidation [68]. Doping of W into $BiVO_4$ was also found useful to increase the photoactivity [70]. Conclusively, the fundamental electronic structure of $BiVO_4$ has not been well explored to date. The reason

is that some authors found $BiVO_4$ as a direct gap semiconductor while some others found $BiVO_4$ as an indirect band gap semiconductor. In particular, it is unclear whether the band gap is direct or indirect and what role the occupied Bi 6s lone pair electrons [75, 91-94] may play in determining the VB edge positions and charge transport properties. Although in the past, many significant and encouraging breakthroughs on $BiVO_4$-based materials have been made, on the basis of both experiments and computation, which provide an important basis for work on highly efficient water oxidation under visible light. Although some discussions focused on $BiVO_4$-based photoanodes for PEC water oxidation can be found in a recent review [95], herein, we focused on the strategies for the rational design and development of $BiVO_4$-based materials for water oxidation. As a whole, further efforts are warranted in the suppression of recombination losses in the $BiVO_4$ bulk, as well as coupling efficient OER co-catalysts to the surface for simultaneous enhancement in catalytic activity and suppression of surface recombination losses. Additionally, systematic efforts in the generation of micro- or nanostructured $BiVO_4$ may produce higher charge-carrier collection efficiencies. Also, it is important to determine the stability limits of $BiVO_4$ in terms of pH and electrochemical potential in aqueous solutions. With regard to success in these areas, $BiVO_4$ may emerge as a very promising metal oxide photoanode material for water oxidation.

3.2 Tungsten Oxide (WO_3)

Tungsten oxide (WO_3) has been the subject of intensive research as a semiconductor anode for water oxidation. WO_3 does not suffer from the unfavorable electronic properties as hematite, as it in crystalline form has reasonably minority carrier lifetimes and isotropic electronic properties. WO_3 is also stable in acidic media. However, a major challenge for WO_3 is its indirect band gap of approximate 2.7 eV, which prevents absorption of a significant fraction

of the solar spectrum.

WO_3 exhibits ABO_3 perovskite-like structure based on the corner-sharing of WO_6 octahedron as shown in Fig. 5 (a) [14]. However, structural analyses of WO_3 have revealed considerable deviations from the ideal cubic perovskite type, the distortions corresponding to antiferroelectric displacements of W atoms and mutual rotations of oxygen octahedral. Pure WO_3 single crystals are thought to exhibit at least five phases in the temperature range 900 to -180^0C, changing through the sequence from triclinic to tetragonal [96-101]. WO_3 displays an important polymorphism as a function of pressure and temperature depending upon distortion and tilting of the corner-sharing octahedral. Interest in the specific case of WO_3 is also stimulated by its catalytic activity toward different reactions [102-104], from the ability to incorporate cations and form insertion compounds (the tungsten bronzes) [105], and form its electronic behavior [106]; it shows in fact ferroelectric, electrochromic, and semiconducting properties. Experimental difficulties arise from the tendency of the solid to form substoichiometric shear phases [107] and twinned crystals [99]; theoretical problems are due to the presence of heavy atom and the low symmetry of the existing structures. Studies on some of WO_3 crystals have been carried out with the non-self-consistent methods [108-111]. Those by Bullet have demonstrated that in the simplified cubic structure, the semiconducting gap is significantly underestimated compared to the monoclinic room temperature structure. The unit cells of different phases of WO_3 and their corresponding band structures are shown in Figs. 5 (b) and (c) respectively [20]. The corresponding experimental and theoretical lattice parameters are summarized in Table I [20] with their respective references.

Table I. Experimental and theoretical Lattice parameters (a, b, c in Å and α, β, γ in degree), and the band gap (E_g in eV), of different phases of WO_3 [20].

			a	**b**	**c**	α	β	γ	E_g
α- WO_3	Experiment	Ref. 96	5.272	3.920					
	Theory	Ref. 20	5.353	3.974					0.61

β- WO_3	Experiment	Ref. 98	7.341	7.570	7.754				
	Theory	Ref. 20	7.519	7.719	7.847				1.27
γ- WO_3	Experiment	Ref. 112	7.327	7.564	7.727		90.49		
	Theory	Ref. 20	7.498	7.649	7.789		90.61		1.40
δ- WO_3	Experiment	Ref. 101	7.309	7.522	7.678	88.81	90.92	90.93	
	Theory	Ref. 20	7.516	7.634	7.788	89.19	90.60	90.63	1.54
ε- WO_3	Experiment	Ref. 113	5.278	5.156	7.664		91.76		
	Theory	Ref. 20	5.358	5.302	7.780		91.31		1.71
orth- WO_3	Experiment	Ref. 114	7.333	7.573	7.740				
	Theory	Ref. 20	7.465	7.668	7.806				1.44
hex- WO_3	Experiment	Ref. 114	7.298		3.899				
	Theory	Ref. 20	7.438		3.827				0.61

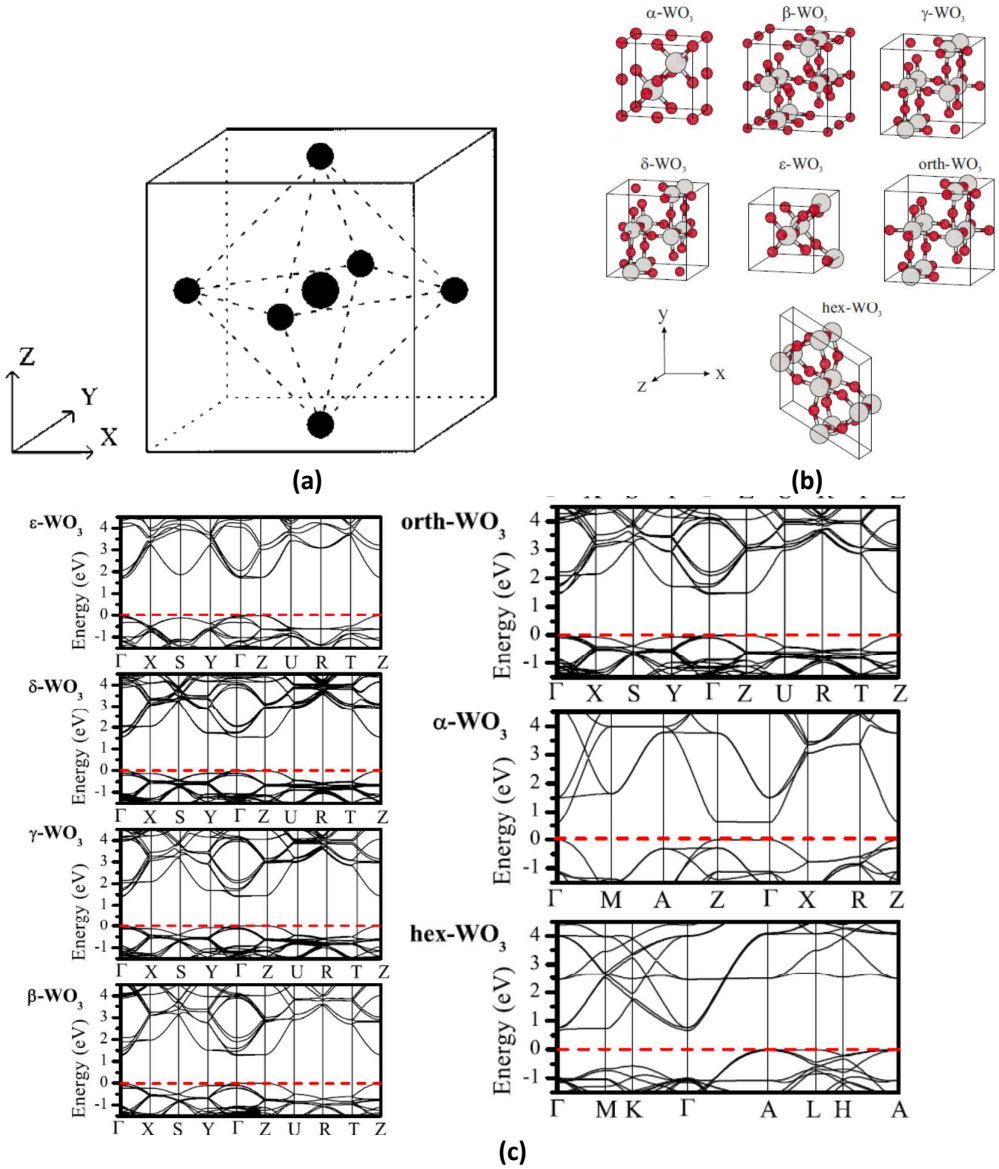

Fig. 5 (a) Cubic perovskite crystal strucrue of WO_3 [14], (b) The unit cells of different phases

of WO_3 [20], and band structures of different phases of WO_3 [20]

Many DFT studies for electronic and optical properties of WO3 have been reported. For example, theoretical investigations by means of ab initio methods have mainly addressed the room temperature γ- WO_3 phase with and without oxygen vacancies [12-14, 115]. In 1983, Bullet et al. [108] has studied the electronic structures of WO_3 in cubic, monoclinic and orthorhombic phases. His results suggested that the detailed crystallographic aarangement determines rather sensitively the size of the semiconducting energy gap, which increases from 1.6 eV in the perovskite-like cubic structure to 2.4 eV in the full monoclinic distorded structure. He also found that surface states are absent from the semiconducting energy gap of the defect (001) surface of WO_3. The extra electrons induced by alkali-metal atoms in the bronzes Na_xWO_3 entered the conduction band of W t_{2g} states, behaving like a rigid-band model. In 1996, Cora and co-workers [17] demonstrated the structural and electronic properties of bulk cubic and tetragonal WO_3 using a periodic boundary condition ab initio HF and DFT methods. The authors found that cubic phase is highly ionic and the symmetry distortion leading to the tetragonal phase causes an increase in covalence between W and its nearest oxygen. The observed instability of cubic WO_3 was explained by its higher energy (0.8 eV per formula unit) with respect to tetragonal phase and even an increase in pressure could not force W ion on-center in its coordination polyhedron. The driving force towards the symmetry breaking was found attributed to the change in the metal-oxygen interaction rather than to effects confined to the metal center alone or to the oxygen-oxygen interaction. In 1999, Wijs and co-workers [14] have studied the several structures of WO_3 with a first-principles psuedopotential method. The authors found that the electronic band gap increases significantly with the distortion of the octahedra that are the building blocks of the various crystal structures and the tilting of the octahedral in the more complex structures leads to a strong increase of the gap upon

compression. In 2003, Pagnier and Pasturel [116] have studied high-pressure polymorphs of WO_3 with a first-principles psuedopotential method. The authors have characterized the medium-range (0.01-20 GPa) and high-range (20-30 GPa) polymorphs and then compared with the experimental results. They found a new feature in the form of appearance of a sevenfold coordinated W in the high-pressure polymorph. In 2005, Ingham and co-workers [18] have performed DFT studies of WO_3, tungsten bronzes, and related systems. WO_3 adopts a variety of structures which can be intercalated with the charged species to alter the electronic properties, thus forming tungsten bronzes. Similar optical effects were observed upon removing oxygen from WO_3, although the electronic properties are slightly different. The authors presented a computational study of cubic and hexagonal alkali bronzes and examined the effects on cell size and band structure as the size of the intercalated ion was increased. $NaWO_3$ was found the most stable cubic systems, although in the hexagonal system, the larger ions were found more stable. In 2008, Huda and co-workers [12] have studied the effects of impurities in room temperature monoclinic WO_3 using DFT-LDA method to demonstrate both substitutional and interstitial cases of nitrogen impurity in WO_3. The authors have also considered transition-metal atom impurities and some co-doping approaches in WO_3. They found that the band gap reduction due to the formation of imprity bands in the band gap. Also, changes of band edge position, VB-maxima and CB-minima were found to depend on the electronic properties of the foreign atom and their concentration. In 2010, Migas and co-workers [20] presented the results of their ab initio calculations indicating that dispersion of the bands near the gap region for different phases of WO_3, such as α- WO_3, β- WO_3, γ- WO_3, δ- WO_3, ε- WO_3, orth- WO_3, and hex- WO_3, is rather close. The rapid increase in the absorption coefficient started at the lower energy for as α- WO_3 and hex- WO_3 than for other phases based on their calculated band gap values. The authors also found that an oxygen vacancy has turned out to

decrease the gap by 0.50 eV and to shift the absorption coefficient to the lower energy range in the room temperature γ- WO_3. The authors have also traced changes caused by Mo and S doping of γ- WO_3 and found that only S doped γ- WO_3 has revealed to display the formation of the impurity band along with a sizable reduction in the gap and the shift in the absorption coefficient to the lower energy range. In 2011, Wang and co-workers [117] applied various hybrid functionals combined with both plane wave and localized basis sets for systematic study of the structural and electronic properties of all phases of WO_3. The authors found that the HSE06 functional in combination with a plane wave basis set describes well the band gap of WO_3, while the B3LYP functional associated with a localized basis set slightly overestimates it. The authors made this band gap fully consistent with experiment by fixing the amount of HF exchange in the hybrid functional to 15%. Moreover, in 2012, Wang and co-workers [118] have studied the electronic properties of doped WO_3 using DFT calculations with hybrid functionals. The authors suggested that the position of the top of the VB in WO_3 is good for O_2 evolution in water splitting; however, the CB is too low for H_2 production and the band gap of WO_3 can be reduced to improve the activity with the visible light by doping of WO_3 with Mo or Cr due to the fact that doping can be used to alter the position of the energy levels, thus resulting in a more efficient photocatalyst. The replacement of W in the lattice by isovalent Mo or Cr ions narrowed the band gap, but shifted the CB edge further down; however, substitution of W with low valent Ti, Zr, or Hf ions widened the band gap and shifted the CB edge to higher energies. In addition, replacing O by S in WO_3 had the effect to narrow the energy gap by introducing localized occupied states above the VB and shifted the CB minimum upward. Thus, both replacing W by Mo or Cr and replacing O by S at the same time showed the right effects. Also, in 2012, Ping and co-workers [119] have studied the structural and electronic properties of WO_3 clatherates with interstitial N_2 molecules ($xN_2.WO_3$, x = 0.034-0.039) using ab initio

calculations and analyzed the physical origin of the gap reduction reported experimentally. The authors found that both structural changes caused by the insertion of N_2 and a small charge overlap between N_2 and WO_3, were responsible for the gap decrease. They also compared the effect of N_2 intercalation to that of other species such as CO and rare gas atoms. Their calculations predicted that CO insertion lowers the band gap by about the same amount as N_2 but it leads to a change of both the oxide VB and CB positions, while the presence of N_2 only affects the CB minimum. They also predicted in case of Xe that a strong hybridization between Xe 5p and O 2p states modifies the VB edge of WO_3, leading to a reduction of the band gap by approximately 1 eV. Moreover, in 2013, Ping and co-workers [120] have performed ab initio calculations of the band structure and absorption spectrum of WO_3 using many-body perturbation theory, taking into account spin-orbit and electron-phonon interaction in order to correctly predict the optical gap of WO_3. The authors found minor differences of approximately 0.05 eV between indirect and direct minimum gap of WO_3, which may explain why different experiments [106, 121, 122] appeared to disagree on the character of the lowest gap of WO_3. Also, in 2014, Ping and Galli [123] have performed first-principles calculations to optimize the band edges of WO_3 for water oxidation. Their calculated results revealed that several phases of WO_3 found either at high energy than that of room temperature monoclinic WO_3 by approximately 0.35 eV and smaller electronic gaps, better suited to efficiently absorb sunlight. They also found that orthorhombic WO_3, stable at high temperature, has improved carrier mobilities for both holes and electrons. The authors proposed that epitaxial growth on appropriate substrates may be a promising way to stabilize metastable phases of WO_3 at ambient conditions in order to improve its photocatalytic activity as photoanode.

Consequently, WO_3 is well-known for its photosensitivity [21-23], good electron transport properties [24], and stability against photocorrosion [25, 26] in acidic aqueous

solutions. Its band gap is smaller than that of the other semiconductors, but still too high to realize a sufficiently large absorption of the solar spectrum [124]; its CB minimum is too low compared to the hydrogen evolution reaction redox potential [125]. Recently, a number of investigations were focused on lowering the band gap of WO_3 by either doping or structural modifications [12, 117, 118, 126-128]. In particular, it was shown that by intercalating small molecules such as N_2, the optical gap of WO_3 can be substantially reduced due to the structural distortion of the WO_6 octahedra, induced by the presence of the guest molecules [119, 129]. The strong dependence of the electronic structure of WO_3 on lattice distortions suggests a possible strategy to reduce the band gap of the monoclinic WO_3. One may deposit the material such as by epitaxy on a suitable substrate favoring the growth of thermodynamically metastable phases [130, 131], which exhibit a smaller band gap than γ-monoclinic WO_3. Alternatively, one could change the morphology of WO_3 such as by synthesizing nanostructured WO_3, including nanowires [132, 133], nanobelts [134], and nanoparticles [135]. In order to improve the catalytic properties of WO_3 for water oxidation, it is necessary not only to decrease its band gap but also to increase the energy of its valence band so as to bring it closer to water oxidation potential and thus, a substantial overpotential is necessary to drive the oxidation reaction [136].

3.3 Hematite (α-Fe_2O_3)

Hematite (α-Fe_2O_3) is readily synthesized from inexpensive materials [137]. To date, sixteen different types of iron oxides are known which differ in composition, oxidation state of Fe, and most important in crystal structure [138, 139]. The diversity in chemical structure and physical properties of the iron oxide phases provide many different applications at the research and industrial levels as shown in Fig. 6 [139]. It has attracted significant research in lithium-ion

batteries [140-142], gas sensors [143, 144], catalysis [145-148], environmental protection [149, 150], and Martian astrochemistry [151-155].

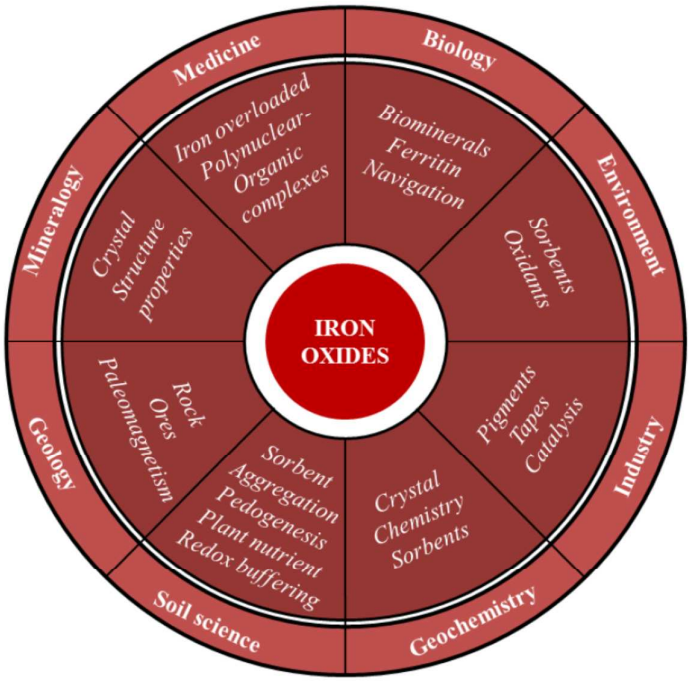

Fig. 6 Scheme of the different scientific disciplines concerned with iron oxides [139]

In particular, hematite is a cost-effective material that has solar cell and photoelectrocatalytic applications [156-158]. There has been a considerable amount of experimental research on hematite regarding its structural, magnetic and electronic properties in bulk [159-177] as well as in nanoparticles [178, 179]. Among the iron oxides, corundum-type α-Fe_2O_3 is the most common at earth. Especially, at high pressure, α-Fe_2O_3 is considered to be of the orthorhombic perovskite type structure, containing Fe^{2+} and Fe^{4+} sites in the same amount [163-165, 169]. Pasternak et al. [125] and Rozenberg et al. [176] assigned the high pressure structure of α-Fe_2O_3 to a distorded corundum-type (Rh_2O_3-II) phase with a single Fe^{3+} cation. Hematite has an indirect band gap of approximately 2 eV [178] and a direct optical gap of 2.7 eV [179], and consequently, presents an exciting opportunity for band gap tuning via doping as it can be

doped n-type. Hematite is stable in electrolyte at pH>3 and it is monotoxic.

From a theoretical point of view, the study of hematite is very attractive due to the challenges it poses to theory. The reason is that the GGA approximation in DFT study underestimates the band gap by 75% as well as incorrectly positions the 3d orbitals such that it predicts a d-d Mott-Hubbard insulator [32]. Standard GGA also underestimates the magnetic moments on the Fe centers. Hematite is an antiferromagnetic insulator below the Neel temperature of T_N = 955 K [160]. At the Morin temperature, T_M = 260 K, there is a magnetic phase transition with antiferromagnetic aligns [180]. Although, there are numerous ab initio studies of NiO, FeO and similar transition metal mono-oxides [181-187], there are a few theoretical works regarding α-Fe_2O_3 [172, 188-192]. Catti et al. [188] have performed HF calculations to achieve the correct order of magnetic states at experimental volume, yielding an energy difference between antiferromagnetic and ferromagnetic alignment of the spins of 37 meV, although they found very weak mixing of Fe 3d and O 2p states. Moreover, the energy gap was overestimated while the predicted bandwidth is too small. Sandratskii et al. [189] have studied α-Fe_2O_3 using conventional local spin density approximation (LSDA) and found antiferromagnetic bilayer sequence for the Fe moments to be lowest in energy (489 meV), being lower than the ferromagnetic state. Punkkinen et al. [190] have calculated the density of states of α-Fe_2O_3 and found that even a modest value of the on-site Coulomb potential improves the prediction for the energy gap without, however, achieving satisfactory agreement for other physical properties.

It is well known that hematite suffers from low electron mobility, low absorption coefficient, high recombination rates, and slow reaction kinetics, leading to small photocurrent density and a sizable overpotential of around 0.5-0.6 V [193-195]. Recently, through doping to increase conductivity, nanostructuring to reduce recombination, and the use of co-catalysts to

improve the surface reaction kinetics, current densities as high as 3 mA/cm^2 were reached with an applied potential of 1.23 V under AM 1.5 illumination [196]. The several factors limiting the performance of hematite photoanode material are connected to the surface properties [193]. The (0001) surface is one of the most stable facets of hematite and thus has been becoming the focus of the extensive research with several conditions such as ranging from fresh, briefly wetted surfaces to dry and humid air conditions or in contact with water and employing various experimental techniques [197-204]. The reason is that several key issues regarding the surface terminations are still not clear. In particular, the relative stability of various surface terminations in contact with water depends on applied voltage [205], pH and temperature. It is thus necessary to determine the stable surface termination through which hematite acts as a photocatalyst for water oxidation. In order to overcome this issue, Norskov and co-workers have performed DFT calculations to model the electrochemical environment [206] and the effect of solar illumination [207, 208] that can provide valuable insights. Moreover, Hellman and Pala [209] have employed PBE exchange and correlation functional to determine the relative stability of the (0001) surface of hematite as a function of the applied bias and modeled the photo-oxidation of water on the most stable surface under solar illumination. On the other hand, Liao et al. [210] have used a DFT + U method to describe the electronic structure of the system and model water oxidation on selected hydroxylated (0001) hematite surfaces. The hexagonal Fe_2O_3 lattice with AFM spin arrangement in ground state and its calculated band structure and partial density of states (p-DOS) are shown in Figs. 7 (a), (b) and (c) respectively [30].

Several previous DFT studies have been done on hematite as a photoanode for water oxidation. For example, in 2004, Rollmann and co-workers [32] have performed DFT studies for rhombohedral α-Fe_2O_3 and found an antiferromagnetic ground state at the experimental

volume, which is 388 meV below the ferromagnetic solution. Their DOS analysis confirmed the

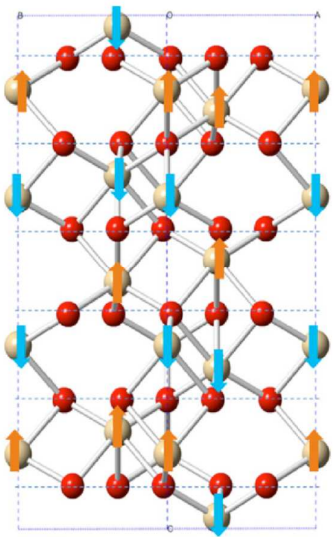

(a)

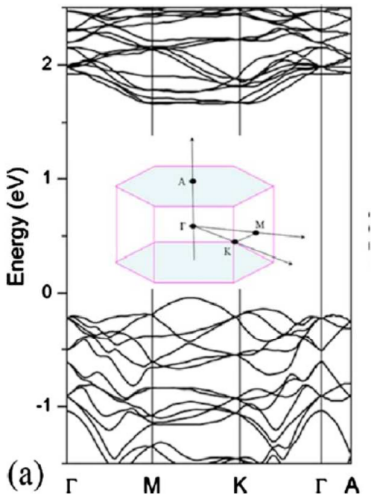

(b)

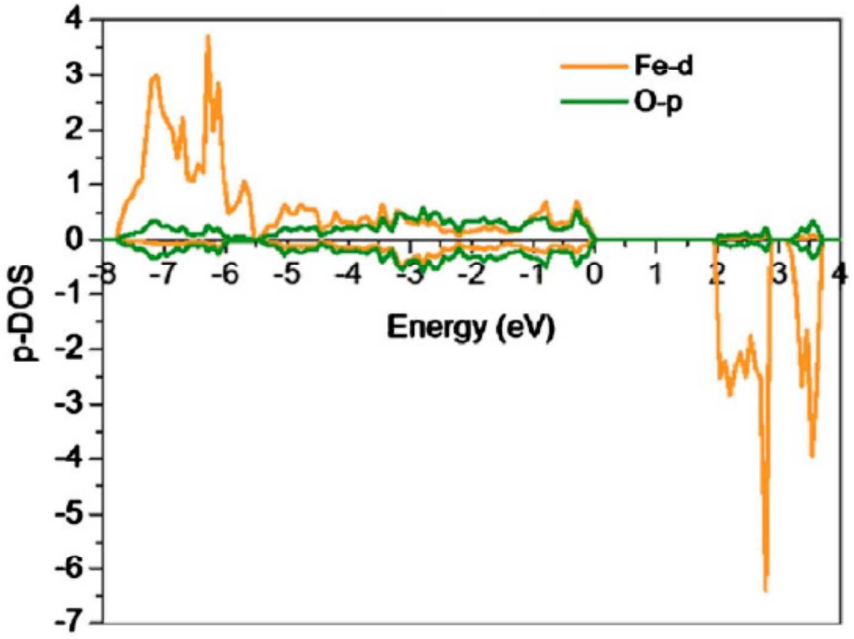

(c)

Fig. 7 (a) Hexagonal Fe_2O_3 lattice with AFM spin arrangement in ground state and its calculated (b) band structure and (c) projected density of states (p-DOS) [30]

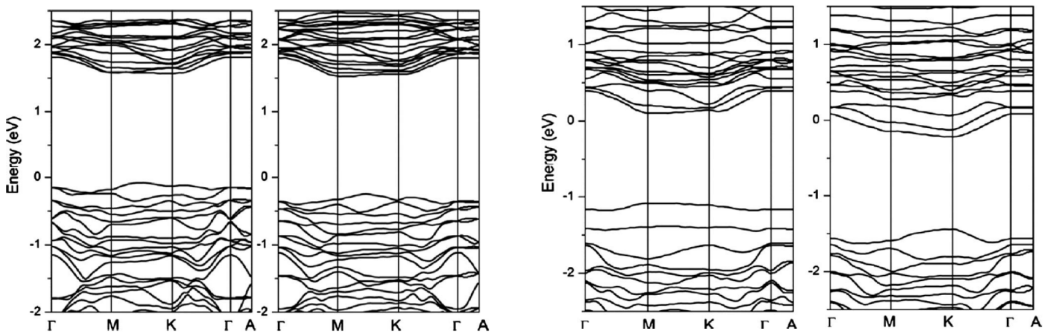
Energy (eV)
Γ M K Γ A

(a) (b)

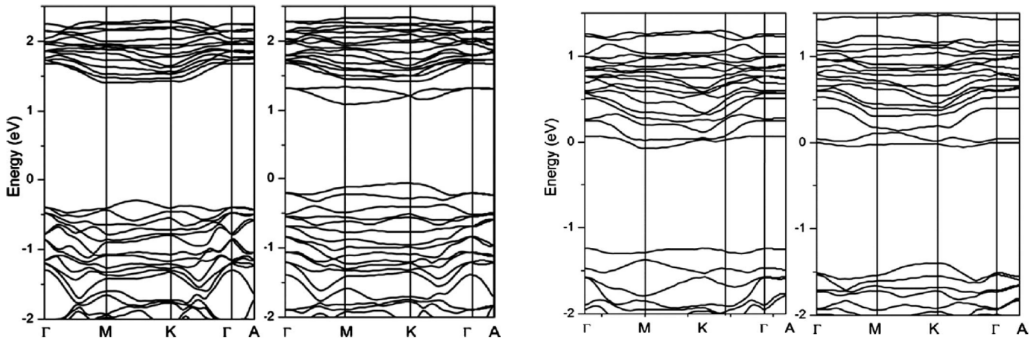
Energy (eV)
Γ M K Γ A

(c) (d)

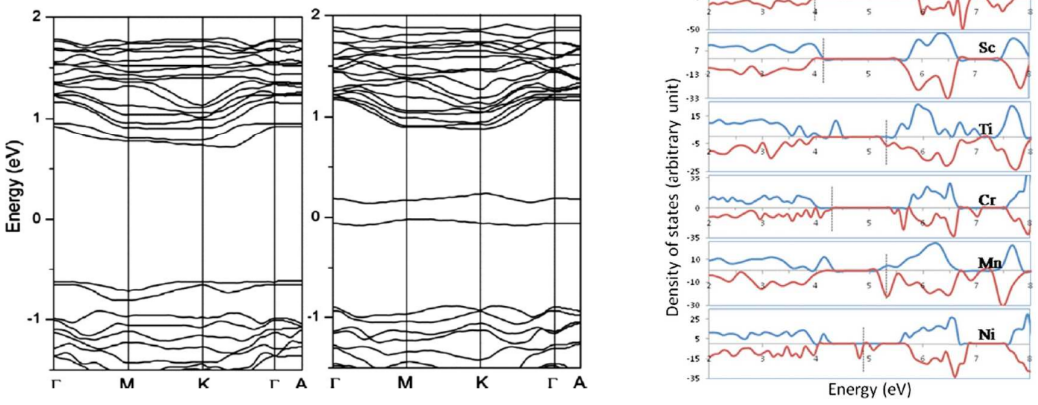
Energy (eV)
Γ M K Γ A
Density of states (arbitrary unit)
Sc
Ti
Cr
Mn
Ni
Energy (eV)

(e) (f)

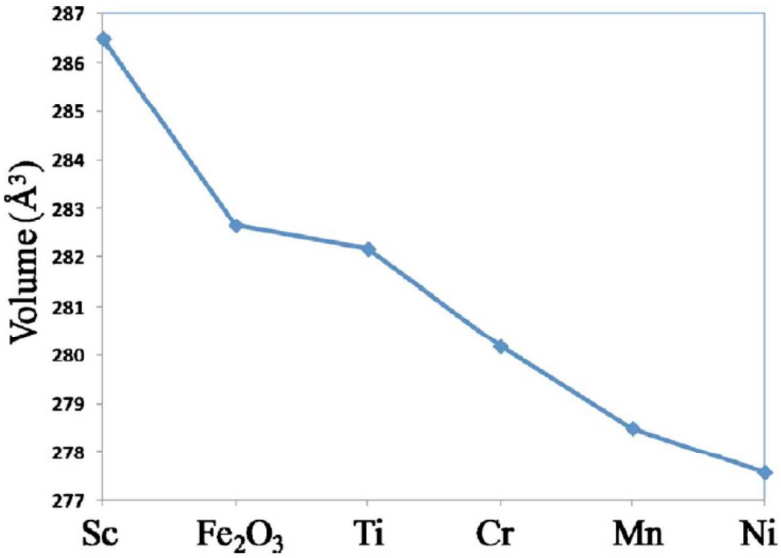

(g)

Fig. 8 Calculated electronic band structures for α-Fe_2O_3: (a) Sc, (b) Ti, (c) Cr, (d) Mn, and (e) Ni, Left panel: spin-up; right panel: spin-down bands; (f) total electronic DOS plot for pure α-Fe_2O_3 and α-Fe_2O_3 incorporated with Sc, Ti, Cr, Mn, and Ni at substitutional sites; and (g) calculated volumes for defective supercells containing 3d transition substitutions in Fe_2O_3 (α-Fe_2O_3) [30]

strong hybridization between Fe 3d and O 2p states in α-Fe_2O_3. The authors have also performed DFT + U calculations to account for the strong on-site Coulomb interaction U present in α-Fe_2O_3 and found that with increasing U, the size of the band gap and magnetic moments increase, while other quantities such as equilibrium value and Fe-Fe distances donot show a monotonic behavior. The best value for U = 4 eV was found sufficient to change the character of the gap from d-d to O-p-Fe-d. In 2010, Huda and co-workers [30] have presented a DFT study on the electronic structure of pure and 3d transition metal (Sc, Ti, Mn, and Ni) incorporated α-Fe_2O_3. They found that the incorporation of 3d transition metals in α-Fe_2O_3 has two main effects such as the VB and CB edges are modified; and the unit cell volume reduces monotonically. In particular, the incorporation of Ti improved the electrical conductivity of α-Fe_2O_3; the incorporation of Sc increased the unit cell volune and of Ti, Cr, Mn, Ni reduced the

volume monotonically, which can affect the hopping probability of localized charge carriers (polarons). The calculated band structures, DOS and volume for defective supercells of α-Fe_2O_3 are shown in Figs 8 (a-g) [30]. Moreover, in 2010, Schwarsctein and co-workers [211] have performed DFT calculations for substitional doping of α-Fe_2O_3 and found that a contraction of the crystal lattice due to isovalent replacement of Fe^{3+} by Al^{3+} benefits the small polaron migration, resulting an improvement in conductivity compared to the undoped α-Fe_2O_3. In 2011, Pozun et al. [212] have presented a hybrid DFT study of doping effects in α-Fe_2O_3. They found that a screened hybrid functional with 12% exact exchange predicts a band gap consistent with experimental observations due to the fact that this functional correctly identifies hematite as a charge transfer rather than the Mott-Hubbard insulator with the proper static dielectric constant and correct uniaxial optical behavior. They have also explored the case of increased doping of Pd into Fe_2O_3 and found correlation with previous experimental results. In 2013, Meng and co-workers [213] have studied the influence of Morin transition on the electronic properties of hematite based on first-principles calculations within the GGA + U framework. They found that comparing the magnitude of electron masses in different Miller planes, the preferential orientation possessing relatively higher electrical conductivity is the (0001) and thus suggested that PEC activity of hematite can be improved by controlling nanostructures with perfect (0001) texture. Sn-doped hematite was found more electrically conductive due to the splitting of CB minima, which is helpful for hydrogen production in PEC water splitting. The calculated orbital projected density of states (PDOS) of pure hematite for both the Morin and zero phases are plotted in Fig. 9 [213], and compared with that of a series of Sn-doped hematite. For pure hematite, the first peak in PDOS was predominated by O-2s bands but with weak Fe-3d states penetrating, which was followed by Fe-O bonding. As a whole the hybridization between O and Fe-3d took place over the whole band, which authors

found in good agreement with the spectroscopic results [170, 214].

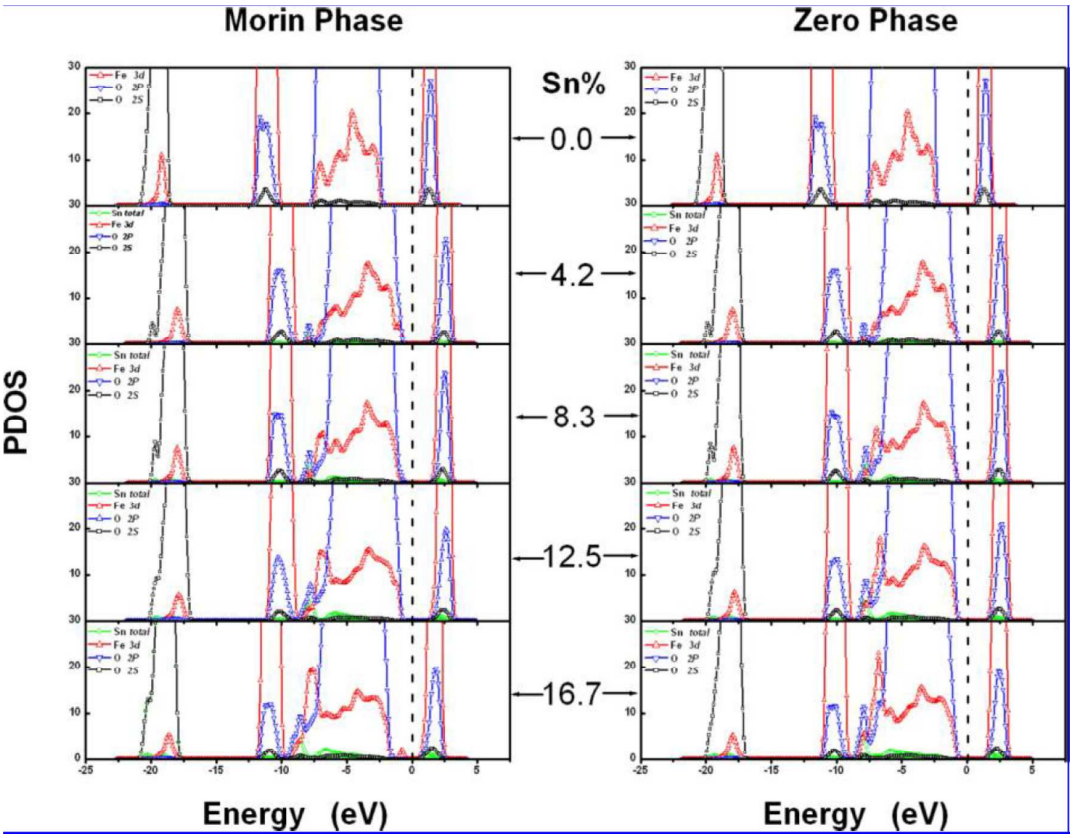

Fig. 9 The GGA + U calculated PDOS of the Sn-doped hematite compared with that of the pure hematite (for both Morin and zero phases). The Fermi level is set to zero. [213]

In 2014, Liu et al. [215] have performed DFT study of mercury adsorption on α-Fe_2O_3 (001) surface in the presence of O_2. Their theoretical calculations indicated that O_2 dissociates in two steps on the surface, leaving one O atom to interact with a surface Fe atom and Hg^0 adsorption on O/ α-Fe_2O_3 (001) surface belongs to weak chemisorption. The authors changed this weak Hg^0 chemisorption into stronger one by increasing O coverage from 0.25 to 1 m^2, with the largest adsorption energy of -268.1 kJ/mol. Moreover, in 2014, Dzade and co-workers [216] have done a DFT study of the adsorption of benzene on α-Fe_2O_3 surfaces and found that adsorption geometries parallel to the surface are energetically more stable than the vertical ones. Their calculated results revealed that the benzene molecule interacts with hematite

surfaces through π-bonding in the parallel adsorption geometries and through weak hydrogen bonds in the vertical geometries. Analyses of the electronic structures revealed that upon benzene adsorption, the CB edge of the surface atoms is shifted towards the valence bands, thereby significantly reducing the band gap and the magnetic moments of the surface Fe atoms. Also, in 2014, Nguyen et al. [217] have conducted a DFT study of photodriven oxidation processes of water on various terminations of the clean hematite (Fe_2O_3) (0001) surface adopting the theoretical scheme developed by Norskov group [218]. They first exposed six best-known terminations, for example, Fe-Fe-O_3-, O-Fe-Fe-, O_2-Fe-Fe-, O_3-Fe-Fe-, Fe-O_3-Fe-, and O-Fe-O_3 to water to investigate photoelectrochemical stability of resulting surfaces (see, Fig. 10 [218]). They also found that the reaction proceeds with a theoretical overpotential of about 0.8 V at pH = 0, with the energetically most demanding step being the oxidation of a Fe-OH group to Fe-O.

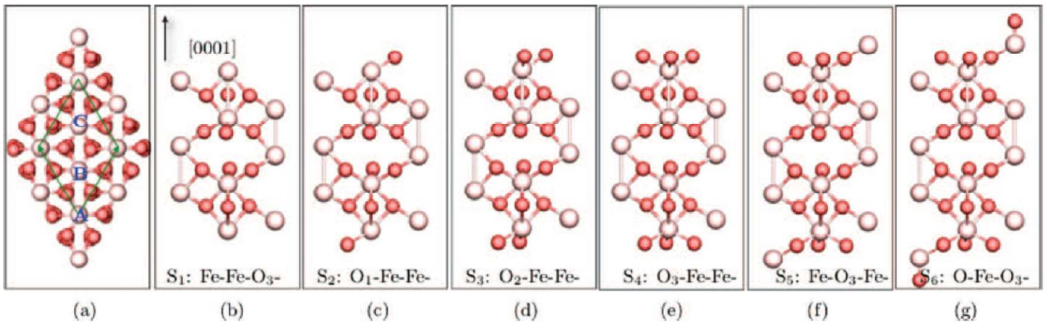

Fig. 10 (a) Top view of 1x1 surface unit cell of the stoichiometric hematite (0001) surface, and (b-g) their six terminations. [218]

In addition, band structure calculations by first principle DFT to better understand the conduction properties of pure been performed by Rosso et al. [219, 220]. For applications to magnetic materials, transition metal doped α-Fe_2O_3 (Sc, Ti, V, Cr, Mn, Fe, Co, Ni, Cu, Zn, and Ga) has been investigated [221] and Ti doped iron oxide was studied theoretically and experimentally by Droubay for its magnetism and conductivity properties [222].

Conclusively, hematite has very promising physical and optical properties and has garnered much research interest as a water splitting photoanode. However, hematite photoanodes have yet to attain sufficient photovoltage (> 1V) or photocurrent density (> 5mA/cm^2) for efficient water oxidation. Although, n-type hematite exhibits potentially good photocatalytic performance, it suffers from a ultrafast recombination of the photo-generated carriers [223]. In addition, the CB edge is below that of the H^+/H_2 redox potential, therefore, spontaneous water splitting under visible light irradiation is not possible, and a voltage bias must be applied [11]. Also, hematite exhibits strongly anisotropic behavior, with electrons and holes traveling more easily along the (001) crystal planes [224]. Such types of difficulties point to the desirability to developing highly nanostructured materials that may permit facile charge carrier collection at the electrolyte interface.

3.4 Tantalum Oxynitride (TaON)

Transition metal oxide photocatalysts have been the subject of most previous studies [10, 225] for their good chemical stability in aqueous solution. However, their relatively large band gap (> 3eV) makes them efficient only under ultraviolet light, which account for only approximate 3% of the solar to hydrogen energy efficiency. In contrast, transition metal nitrides usually have a smaller band gap than the corresponding oxides, but their easier oxidation in aqueous solution threatens to degrade them quickly [10, 51, 52]. In this way, in between the oxides and nitrides, tantalum oxynitride (TaON) has a band gap around 2.5 eV, between those of Ta_2O_5 (3.9 eV) and Ta_3N_5 (2.1 eV), is found to have high quantum yield for nonsacrificial visible-light-driven water splitting [53-55]. The properties of TaON are known to be predominantly influenced by the amount of nitrogen incorporated into the oxide or of the oxygen introduced into the nitride [225], which greatly influences the tunable or controllable

properties by varying the oxygen: nitrogen ratio [226-228]. Moreover, TaON has appropriate alignment of its VB and CB edges relative to the OH^-/O_2 oxidation and H^+/H_2 reduction potentials, make it possible to produce H_2 and O_2 from water even without an externally applied bias [51, 55]. The unit cell structure of TaON and its calculated band structure are shown in Figs. 11 (a) and (b-i, ii) respectively [56].

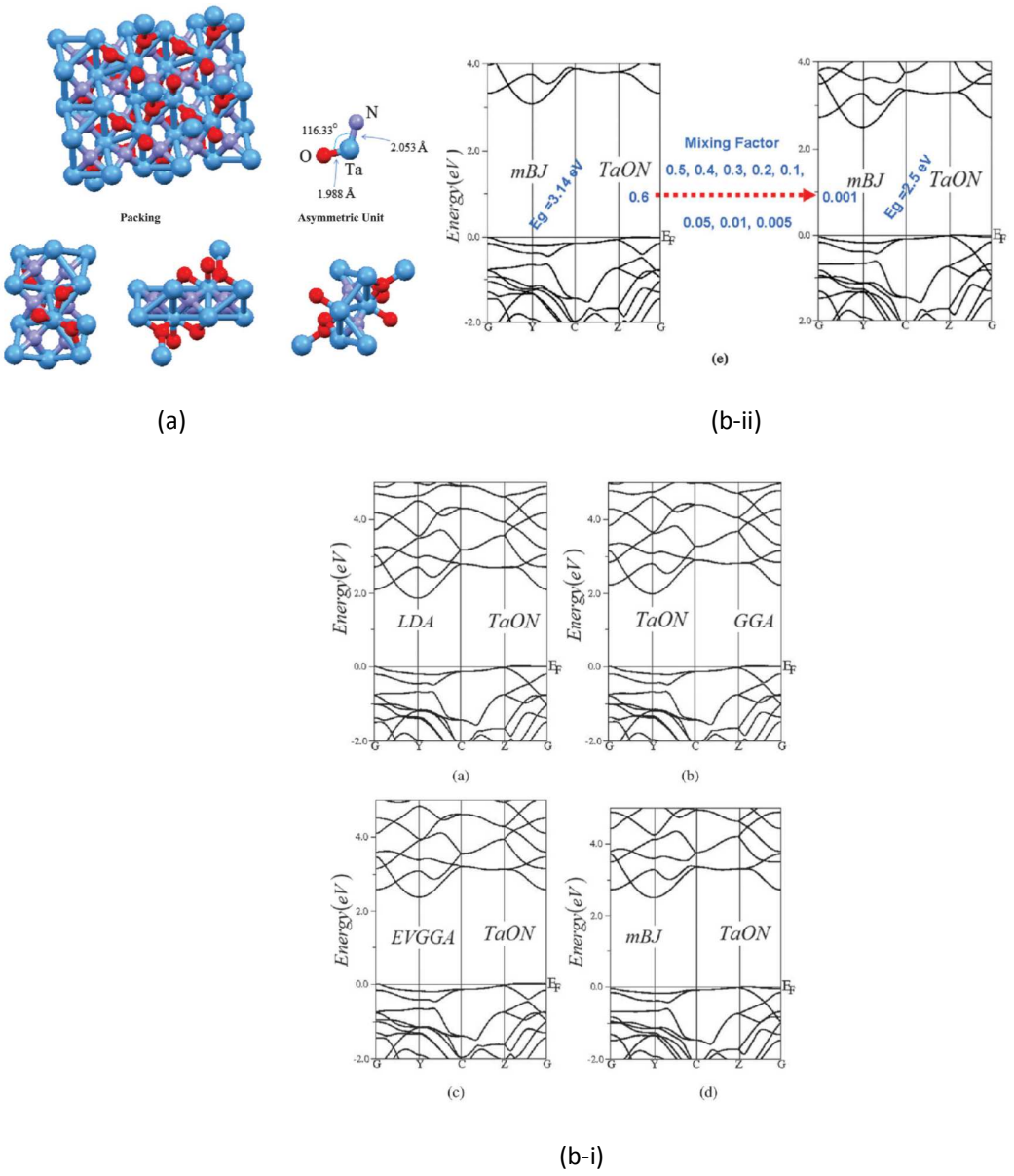

Fig. 11 (a) Unit cell structure of TaON and (b-I,ii) calculated band structures of TaON. [56]

The only stable crystal of TaON is a monoclinic baddeleyite structure with space group $P2_1/C$ as shown in Fig. 11 (a) [56]. Oredred arrangements of anions occurred in alternate layers of OTa_3 (triangles) and NTa_4 (tetrahedral) [56]. From Fig. 11 (b-i, ii), one can see that the CB minimum is located at point γ of the Brilluoin zone, while the VB minimum is located at the center of Brilluoin zone, resulting in an indirect band gap.

Despite the experimental progress in the photocatalytic performance of TaON, it is still not well understood what intrinsic defects contribute to the observed n-type conductivity [53, 229]. Previous studies reported that the defects related to the anion vacancies or reduced Ta may be the origin of the observed n-type character [53], but no detailed study was reported for energetical formation of these defects. On other hand, we require both n- and p-type semiconductors as photoanodes and photocathodes for O_2 and H_2 evolution under Z-scheme water splitting [50, 53, 54]. Therefore, the ability to dope TaON to n- or p-type becomes important. It is well known that most experiment observed only n-type conductivity in TaON for O_2 evolution than for H_2 evolution [51, 55] and it is not clear if p-type doping is possible. Brauer and Weidlein [230] have discussed tantalum oxynitride. The confirmed and stable polymorph of TaON is only the monoclinic baddeleyite structure β-TaON, in which the ordered arrangement of O and N was observed using a powder neutron diffraction method [231]. The existing α-TaON hexagonal polymorph proposed by Buslaev et al. [232] was rejected on the basis of quantum mechanical calculations [233]. A metastable polymorph, γ-TaON, is a new phase proposed by Schilling et al. [234].

A few theoretical studies [56-60] have been published on the electronic structure of TaON and Ta_3N_5, and a recent study [235] appeared on O-doped Ta_3N_5. Using the DFT-GGA approach, Fang et al. [57] initially calculated the density of states of TaON and Ta_3N_5 and they reported band gaps of 1.8 and 1.1 eV respectively. Later, Yashima et al. [56] reported the DOS

of TaON calculated using the DFT-PBE method with a band gap of 2.1 eV. Moreover, Li et al. [60] showed a DOS of TaON calculated using the DFT-LDA method with a band gap of 1.92 eV. Although DFT-LDA and DFT-GGA methods give very good structural results of semiconductors, they are well documented to strongly underestimate their band gaps [236, 237], which are instead more accurately calculated using recent hybrid functionals such as HSE06 [237-241]. TaON can be excited for photocatalysis at wavelengths upto 530 nm and calculated band gap is 2.3 eV [228, 242-244]. Chun et al. [244] used X-ray, ultraviolet photoelectron spectroscopy (UPS) and electrochemical analysis to find the band position of TaON. Orhan et al. [245] studied the synthesis and energetics of the yellow TaON; the diffuse reflectance spectra showed that the measured band gap is 2.4 eV. Al-Aqtash et al. [246] reported the results of ab initio studies of the electronic structure of TaON-based alloys. They showed that the position of the VB and CB can be modified by varying the oxygen and nitrogen concentrations in $TaO_{1-x}N_{1+x}$. They found that the static refractive index of TaON has a value of 2.47, which is similar to the experimental results (2.5 at 632.8 nm wavelength) for TaON films. In 2011, Chen and Wang [247] have performed DFT calculations to investigate the phase stability, the formation of intrinsic defects and their influences on the electronic conductivity of TaON and found that stoichiometric TaON is observed to be stable under a relatively O poor condition and can be easily oxidized due to the easy formation of O_N antisites; however, with the deep donor states associated with the O and N vacancies, the donor state of the O_N antisite is shallow and has a delocalized distribution, indicating a better electronic conductivity in TaON compared to Ta_2O_5 and Ta_3N_5. In 2012, Chihi et al. [248] have performed ab initio calculations to investigate the structural and electronic properties of pure Ta, TaON, and ZrTaON. The authors found that the large total density of states for ZrTaON implies the highest electronic conductivity. In addition, no strong interaction between Ta and (O, N) was found in TaON compound, but Zr increased

this interaction in ZrTaON compound. Moreover, in 2012, Abbondanza and Meda [249] have performed DFT studies to investigate the electronic and structural properties of crystalline materials based on β-TaON (baddeleyite-type). They found that the β-form of TaON is an n-type semiconductor when O prevails, while is a p-type semiconductor when N prevails. The authors have found the best stable structure when Ta-vacancy was formed in conjunction to an O increase. In 2013, Wang et al. [250] have studied hierarchical metastable γ-TaON hollow structures for efficient visible-light water splitting using both experimental and theoretical techniques. They found the order of phase formation as Ta_2O_5 ⟶ γ-TaON ⟶ β-TaON ⟶ Ta_3N_5.

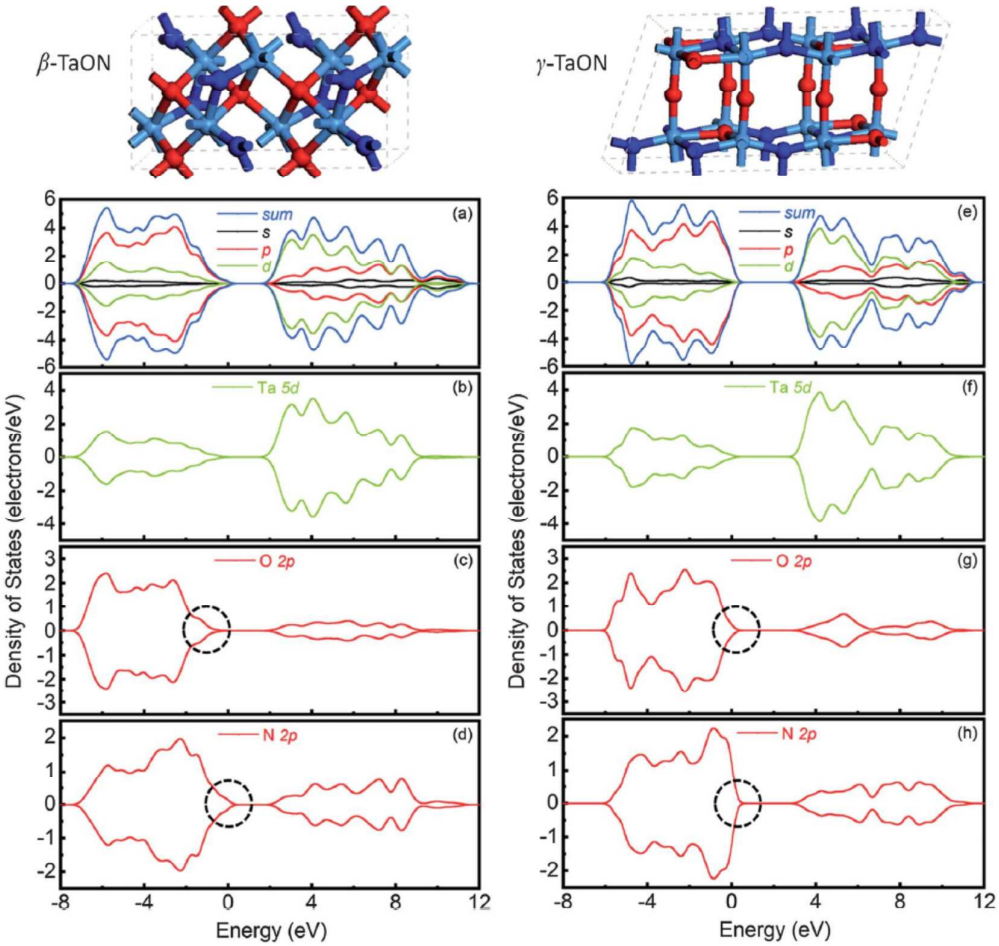

Fig. 12 Calculated density of states (DOS) of (a-d) β-TaON and (e-h) γ-TaON. [250]

In addition, the combined effect of the crystal and electronic structures and hierarchical morphology on the tunable photocatalytic and photoelectrochemical performances of the tantalum-based photocatalyst was systematically investigated. The excellent photocatalytic activity was attributed to the unique urchin-like nanostructure with large specific surface area, the metastable structure and appropriate electronic structure as well as the efficient charge carrier separation. The calculated density of states (DOS) of β-TaON and γ-TaON are shown in Figs. 12 (a-d) and (e-h) respectively [250]. The calculated band gaps showed that the band gap of γ-TaON is slightly higher than that of β-TaON, Ta 5p states contributed mainly to the CB and O 2p and N 2p states to the VB. For γ-TaON, it was found that, although the VB maximum mainly consists of O 2p and N 2p orbitals, better hybridization occurs at the VB maximum in γ-TaON between O 2p and N 2p states than in β-TaON as shown in Fig. 12 (g) and (h) and results in band gaps larger than β-TaON, which corresponds to the UV absorption spectrum [251]. It was considered by authors [250] that the electronic structure of γ-TaON contributes to the higher activity of the photocatalyst, even though the absorption band edge of the solid solution is located at a wavelength 100 nm shorter than that for β-TaON. Moreover, in 2014, Harb et al. [252] have performed DFT calculations with the screened non-local hybrid HSE06 functional for tuning the properties of visible-light-responsive tantalum oxynitride photocatalysts by non-stoichiometric compositions. They considered O-enriched Ta_3N_5 and N-enriched TaON materials. Although, their structural parameters were found to be very similar to those of pure compounds and in good agreement with available experimental studies, their photocatalytic features for visible-light-driven overall water splitting reactions showed different behaviors. They predicted Ta_3N_5 to be a good candidate for H_2 evolution and TaON to be a good candidate for water oxidation and O_2 evolution. Among the various explored $Ta_{3-x}O_{5x}N_{5-5x}$ structures, a strong stabilization was obtained for the configuration displaying a

strong interaction between the O-impurities and the created Ta-vacancies. In the lowest energy structure, each created Ta-vacancy was found to be surrounded by O-impurity species substituting the five N sites characterizing octahedral environment.

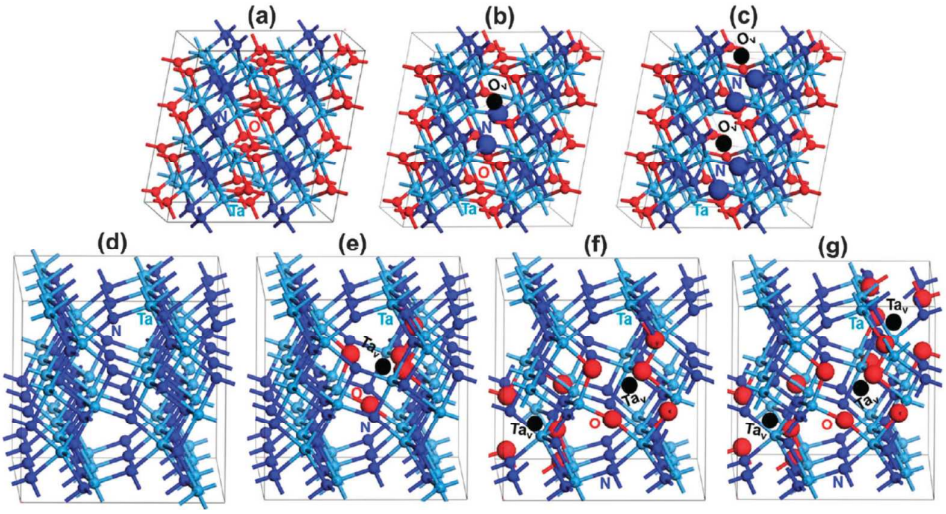

(i)

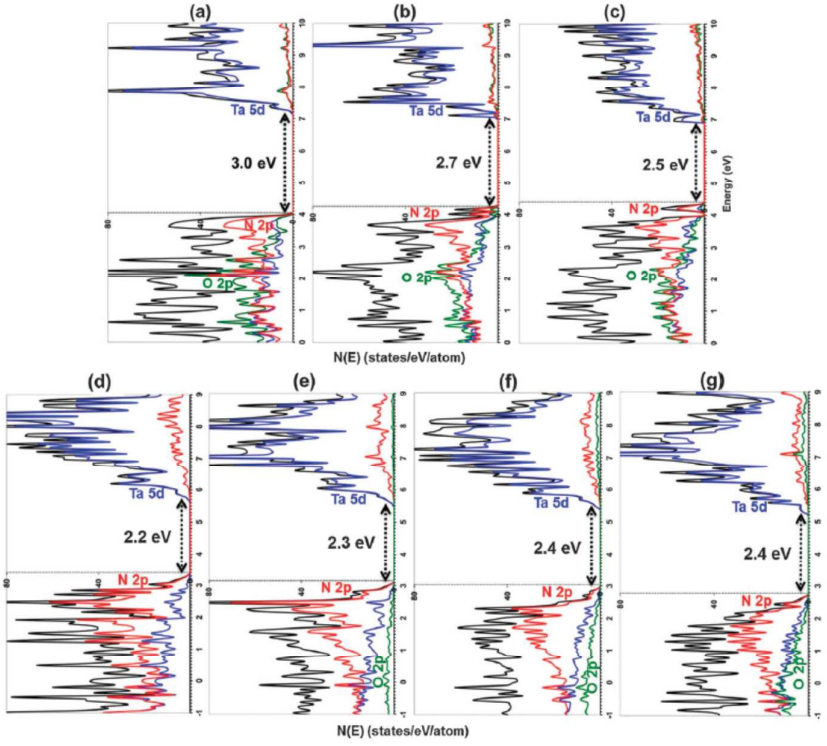

(ii)

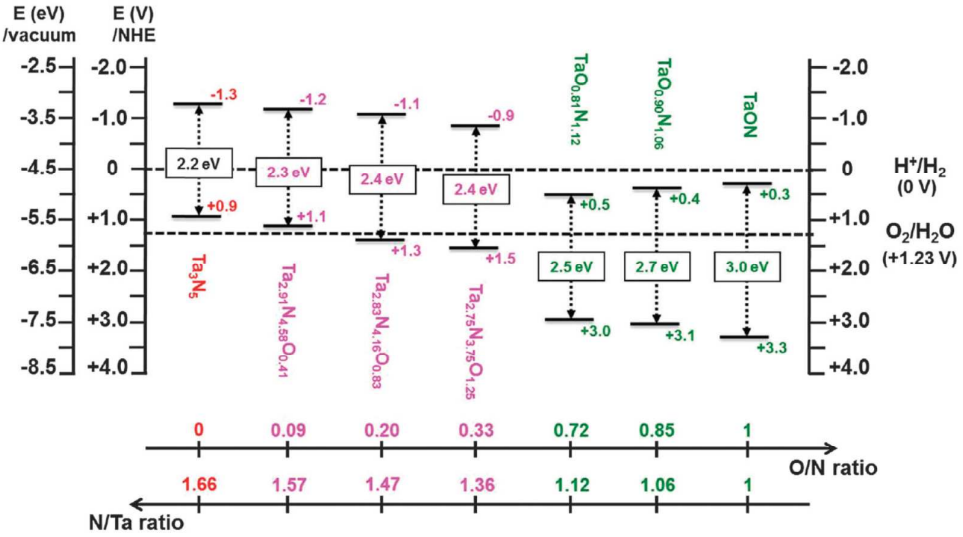

(iii)

Fig. 13 (i) DFT-optimized lowest energy structures of various explored materials obtained using the DFT-PBE method, (ii) their calculated electronic density of states (DOS) using the DFT-HSE06 method, and (iii) the calculated VB and CB edge positions of the various explored materials using the DFT-HSE06 method. [252]

DFT-optimized lowest energy structures of various explored materials obtained using the DFT-PBE method, their calculated electronic density of states (DOS) using the DFT-HSE06 method and the calculated VB and CB edge positions of the various explored materials using the DFT-HSE06 method are shown in Figs. 13 (i-iii) [252]. Also, in 2014, Reshak et al. [253] has done ab initio study of TaON under visible light irradiation and found that the calculated band gap value obtained by modified Becke-Johnson potential approximation (2.5 eV) is very close to the experimental result (2.5 eV). The author proposed that the hybridization among the Ta-d, O-p and N-p states resuls in the formation of a covalent bond between Ta-N and Ta-O. He found that TaON has dielectric constant, anisotropy in the energy range between 3.0 eV and 10.0 eV, and a high refractive index of 2.47 at 632.8 nm.

Conclusively, adequate band gaps (around 2.4 eV), absorption extension towards the visible range (550 nm) and good stability in aggressive environments, make Ta-based

oxynitrides quite interesting. Unfortunately, it is impossible to distinguish O and N atoms on the basis of XRD data so that DFT calculations can give indication on what happens when both site occupancies and stoichiometry are changed [255, 256]. The experimental and theoretical studies to date could not make clear about the photocatalytic behavior of TaON. Therefore, further investigations about the stability of the crystal with different stoichiometries have to be considered. More DFT calculations should be devoted in this direction.

3.5 Tantalum Nitride (Ta_3N_5)

In order to improve the solar energy conversion efficiency, harnessing visible light for photocatalytic water splitting is inevitable and has been developed using various approaches [255-257]. In number of studies, various metal oxynitrides have been reported to be active photocatalysts for H_2 or O_2 evolution in the presence of suitable sacrificial reagents [51, 256, 258]. Among these materials, tantalum nitride (Ta_3N_5) has received considerable attention over the past years for its small band gap (approx. 2.1 eV) [243, 244, 259-261]. In particular, recent electrochemical and spectroscopic measurements have shown that the CB and VB of straddle the H^+/H_2O and O_2/H_2O redox potentials [244], possibly allowing Ta_3N_5 to perform unassisted water splitting. Moreover, considering complete absorption and 100% utilization of photons with higher energy than the band gap, Ta_3N_5 could exhibit a photocurrent 12.5 mA/cm^2 [262]. However, photoelectrochemical measurements of several in different conditions have reported photocurrents less than $7mA/cm^2$, even with an applied bias in the presence of electrocatalysts [263, 264].

A few theoretical studies [57-59] were reported for density of states of Ta_3N_5 calculated by using DFT-LDA and DFT-GGA methods, and respective band gaps of 1.5 eV and 1.1 eV were estimated. These two standard DFT methods strongly underestimate the band

gaps of semiconductors [236, 237]. To overcome this scarcity, DFT method using HSE06 functional was found useful [237-241]. However, no DFT-HSE06 studies for optical absorption and the band edge positions of Ta_3N_5 relative to water redox potentials were reported. In 2014, Harb et al. [265] have performed DFT calculations within the screened Coulomb hybrid (HSE06) functional to study relevant properties of visible-light overall water splitting reactions of perfect and self-defective bulk Ta_3N_5 semiconductor photocatalysts. Among the various explored self-defective structures, a strong stabilization was obtained for the configuration displaying a direct interaction between the created N- and Ta-vacancies. In the lowest-energy structure, each of the three created Ta-vacancies and the five created N-vacanices was found to be aggregated disposition, resulting to the formation of cages into the lattice. The authors predicted the band gap of the the perfect and that of self-defective Ta_3N_5 to be 2.0 eV. This calculated results revealed that the perfect Ta_3N_5 is suitable for H^+ reduction while self-defective Ta_3N_5 is suitable for both water oxidation and H^+ reduction similar to the experimental data reported on Ta_3N_5 powders. The lowest-energy and metastable structures obtained with PBE for pure $Ta_3N_5$and self-defective Ta_3N_5 are shown as in Fig. 14 (i) (a-c) [265]. The calculated density of states (DOS) for the optimized lowest-energy structure and UV-Vis optical absorption spectra obtained with HSE06 for pure $Ta_3N_5$and self-defective Ta_3N_5 are shown as in Fig. 14 (ii) (a-c) [265]. The DOS analysis revealed that a VB dominated by filled N 2p states and a CB governed by fully empty Ta 5d states. The lowest energy band gap in Ta_3N_5 involved transitions between N $2p^6$ orbitals and Ta $5d^0$ orbitals. The calculated UV-Vis optical absorption spectrum showed a broad absorption edge extending upto 564 nm (see, Fig. 14 (ii) (c)). The VB and CB edges of the self-defective Ta_3N_5 were found completely different from those of perfect one, and consequently, different photocatalytic behavior was expected.

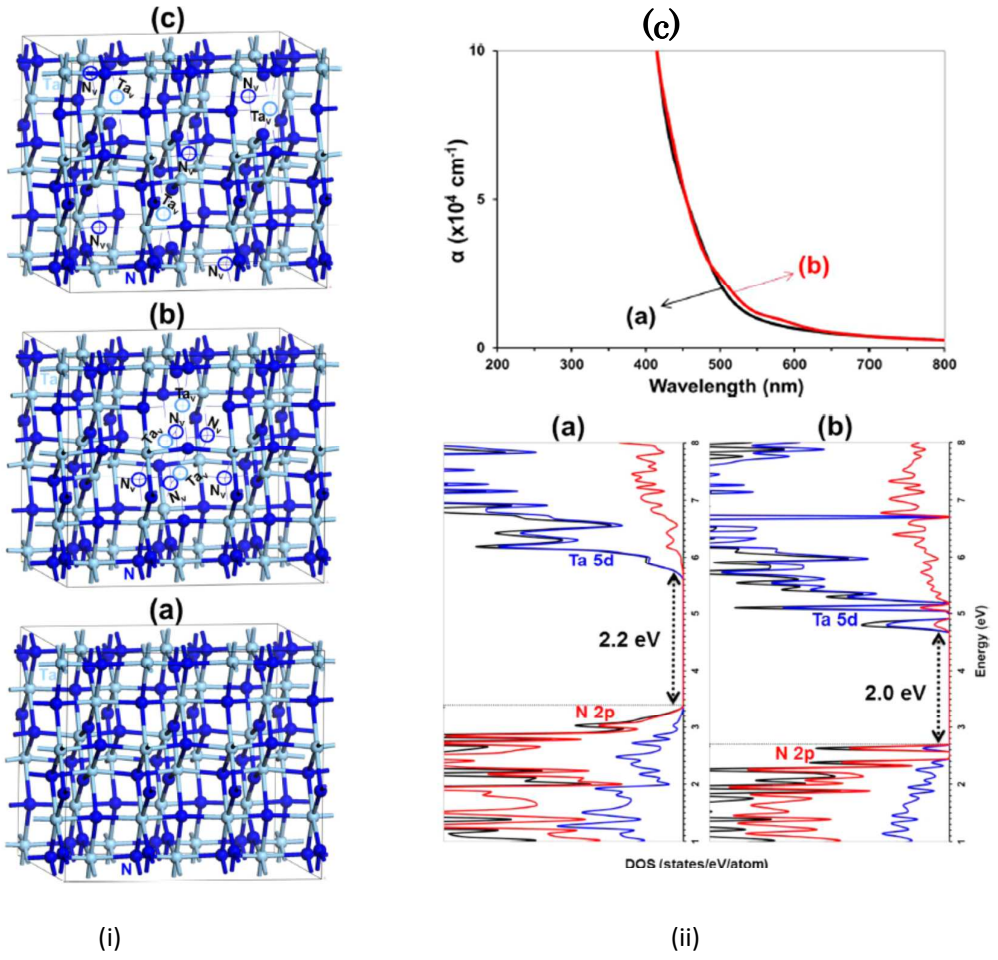

Fig. 14 (i) DFT-optimized lowest energy structure and metastable structures of pure Ta_3N_5 obtained using the DFT-PBE method: (a) perfect material and (b) self-defective material with aggregated N- and Ta-vacancies, and (c) self-defective material with separated N- and Ta-vacancies, and (ii) their calculated electronic density of states (DOS): (a) perfect Ta_3N_5 and (b) self-defective Ta_3N_5 with aggregated N- and Ta-vacancies, and (c) UV-Vis optical absorption spectra for perfect Ta_3N_5 and self-defective Ta_3N_5 with aggregated N- and Ta-vacancies, using the DFT-HSE06. [265]

Moreover, in 2014, Nurlaela et al. [266] have studied the critical role of the semiconductor-electrolyte interface in photocatalytic performance for water splitting reactions using Ta_3N_5 particles by means of both experimental and theoretical techniques. DFT calculations based on partially oxidized $Ta_3N_{4.83}O_{0.17}$ and N-deficient $Ta_3N_{4.83}$ consisting of reduced Ta-species well described the optoelectrochemical properties obtained from

experiments. DFT-optimized lowest-energy structure obtained for Ta_3N_5, $Ta_3N_{4.83}O_{0.17}$ and $Ta_3N_{4.83}$; their electronic density of states; and UV-Vis optical absorption spectra, calculated using the DFT-HSE06 method are shown in Figs. 15 (i-iii).

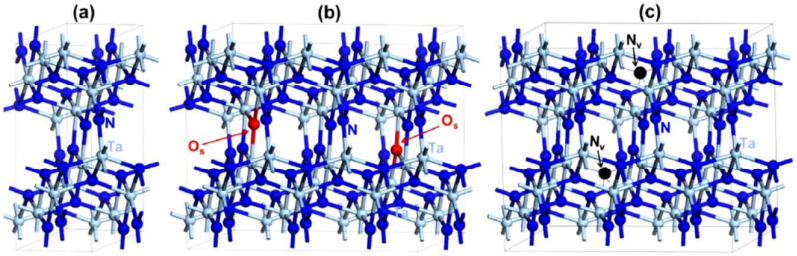

(i)

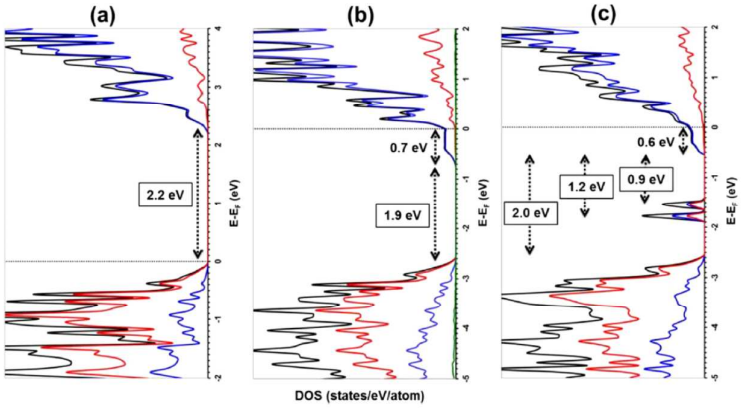

(ii)

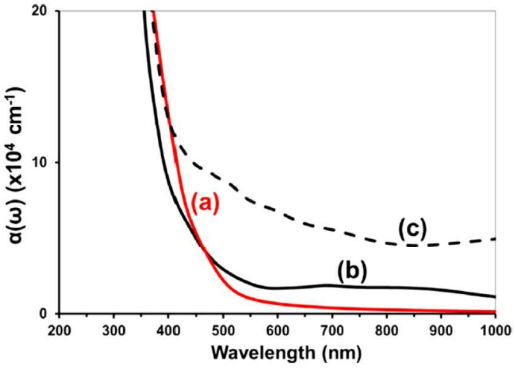

(iii)

Fig. 15 (i) DFT-optimized lowest energy structure, (ii) electronic density of states, and (iii) UV-Vis optical absorption spectra, calculated using DFT-HSE06 method for: (a) Ta_3N_5, $Ta_3N_{4.83}O_{0.17}$ and $Ta_3N_{4.83}$. [266]

As shown in Fig. 15 (iii) (a), the calculated DOS for (N/Ta: 1.66) predicted a band gap of 2.2 eV. The VB governed by occupied N 2p orbitals, whereas the CB was mainly composed of empty Ta 5d orbitals. The UV-Vis absorption spectra revealed an absorption onset at 565 nm (see Fig. 15 (iii) (a)). The lowest energy band gap in this compound involved transition between N $2p^6$ orbitals and Ta $5d^0$ orbitals. For $Ta_3N_{4.83}O_{0.17}$ (O/N = 0.035, N/Ta = 1.61) material, the DOS revealed an n-type conductivity, resulting from the appearance of new deep donor metallic states located within the 0.7 eV range just below the original CB edge of pure Ta_3N_5 and the VB consists of fully occupied N 2p orbitals. The electronic excitations the deep metallic states to the empty Ta 5d states located within the 0.6 eV above the bottom of the original CB edge of pure Ta_3N_5 are at the origin of the new low-intensity broad absorption bands that appeared at wavelengths greater than 565 nm. For $Ta_3N_{4.83}$ (N/Ta = 1.61) material, the calculated DOS showed an n-type conductivity originating from the presence of new deep donor metallic states formed by Ta 5d orbitals and located within the 0.6 eV range just below the original CB edge of pure Ta_3N_5. Similar to pure Ta_3N_5, the VB edge is governed by fully occupied and delocalized N 2p orbitals, whereas the CB edge is mainly composed of completely empty and delocalized Ta 5d states in the original CB of pure Ta_3N_5 lead to a different optical behavior with new high intensity, very broad absorption features that extend to higher wavelengths. Also, in 2014, Morbec et al. [267] have performed a joint theoretical and experimental study of the optoelectronic properties of Ta_3N_5 by means of ab initio calculations and ellipsometry measurements. The calculated optical gap (2.06 eV) computed from G_0W_0 photoemission gap, taking into account spin-orbit coupling, exciton binding energy, and electron-phonon interaction, compared very well with the measured value of 2.1 eV. The authors found that Ta_3N_5 has an indirect gap about 0.2-0.3 eV lower than its smallest direct gap. Their theoretical results also showed that a highly anisotropic material with large electron and hole effective

masses in certain directions, indicating that this material may have low mobilities consistent with photocurrents in the literature that are well below the optical limit. In particulat, they found that holes are in general heavier than electrons, consistent with the experimental findings [268]. The crystal structure of Ta_3N_5, its band structure, partial and total density of states, obtained using DFT-PBE at the experimental geometry is shown in Fig. 16 (a-c) [267]. The Ta_3N_5 crystal has an orthorhombic structure with space group Cmcm. The conventional unit cell consists of 32 atoms, where each Ta atom is bonded to six N atoms, while N atoms have three or four Ta atoms (see, Fig. 16 (a)). The VB maximum is located at the Γ-point and the CB minimum is located at Y-point (see Fig. 16 (b)). The density of states displayed in Fig. 16 (c) shows that the top of the VB is mainly composed of N2p orbitals, while the bottom of the CB is mainly composed of Ta 5d orbitals; which is in agreement with previous work [57, 235, 267], indicating that the transitions near the absorption edge occur between N 2p and Ta 5d orbitals.

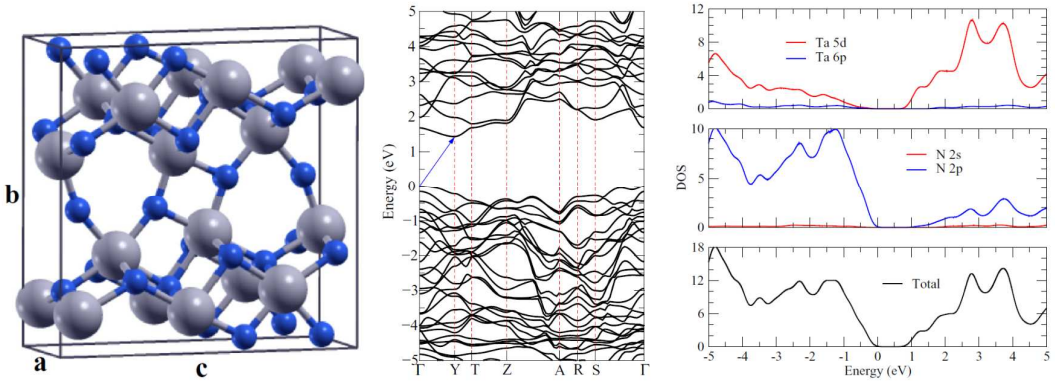

(a) (b) (c)

Fig. 16 (i) Crystal structure of Ta_3N_5, (ii) its calculated band structure, and (iii) partial and total density of states, using DFT-PBE method at the experimental geometry. [267]

Consequently, Ta_3N_5 has received considerable attention over the past years for its small band gap of about 2.1 eV. Although, this key parameter is important to absorb a wide range of visible light which counts for 43% of the solar radiation, two additional challenging

parameters must also be justified in the semiconductor photocatalyst for achieving efficient solar water splitting: (i) suitable CB and VB edge positions relative to water redox potentials to provide the driving force to the photogenerated holes and electrons to oxidize water and to reduce H^+; and (ii) strongly delocalized electronic characters of the band edge states to minimize the electron-hole recombination in the bulk and to assist for their required mobility to the reactive sites at the surface.

4. Development of DFT Methods for Designing Efficient Photoanodes

The DFT methods have been very successful in explaining experiments and predicting material's properties. But there are several approximations for the exchange-correlation functional and at the same time the Kohn-Sham DFT method is a mean field approach. In order to design an efficient material for water splitting photoanode, the structural, electrical, and optical properties of the material has to be carefully studied. In this regard, the DFT is a very powerful tool that can provide a deep understanding about the structural, electrical, and optical properties of the photoanode material. But, at the same time, DFT functionals such as LDA and GGA underestimates the bandgap of photoanode materials. For example, Nashed et al. [269] studied the band structure of β-, δ-Ta_2O_5, and their proposed structure (re-oriented β-Ta_2O_5) using DFT methods with GGA-PBE and three hybrid functionals namely HSE06, B3LYP, and PBE0. Their calculated results found the bandgaps of all three structures of Ta_2O_5 as 0.2, 1.04, and 1.45 eV (GGA-PBE); 2.15, 2.65, and 2.71 eV (B3LYP); and 2.45, 2.92, and 3.7 eV (PBE0) respectively. The experimental bandgap of Ta_2O_5 was reported to be in the range 3.7-4.0 eV [27-272]. The error between the GGA-PBE bandgap and experimental bandgap is found to be 95%. The authors of this paper can be reduced this error to 5% by chosing the re-oriented β-Ta_2O_5 and hybrid functional PBE0. Moreover, Wu et al. have previously used HSE06 functional

to calculate the bandgap of Ta_2O_5 [273, 274]. However, they reported bandgaps of only 0.9 eV and 2.0 eV for β- and δ-Ta_2O_5, respectively [275]. This corresponds to an error of 77% for β-Ta_2O_5 and 49% for δ-Ta_2O_5, compared to experimental bandgap. The improved results upon the use of PBE0 compared to HSE06 may be due the fact that the exchange energy for HSE06 has less HF exchange fraction than PBE0. As HF reduces the self-interaction error of the density functional [276], PBE0 is expected to give more accurate results than HSE06. The exchange – correlation expression (E_{XC}) for PBE0 is given by

$$E_{XC}^{PBE0} = \frac{1}{4}E_X^{HF} + \frac{3}{4}E_X^{PBE} + E_C^{PBE} \quad \text{..... (6)}$$

where E_X^{HF} is the HF exchange energy and $E_X^{PBE}\ and\ E_C^{PBE}$ are the exchange and correlation energies based on the PBE functional. In HSE06, the E_{XC} splits into two regions: short range and long range, with a parameter ω that determines the separation range. Only the short range part is a mixture of HF and the PBE functional, whereas the long range includes PBE only. The expression for E_{XC} for HSE06 is given by

$$E_{XC}^{HSE} = \frac{1}{4}E_X^{HF,SR}(\omega) + \frac{3}{4}E_X^{PBE,SR}(\omega) + E_X^{PBE,LR}(\omega) + E_C^{PBE} \quad \text{..... (7)}$$

where $E_X^{HF,SR}(\omega)$ is the short range exchange energy based on HF calculations, $E_X^{PBE,SR}(\omega)\ and\ E_X^{PBE,LR}(\omega)$ are the short range and long range PBE exchange energies, respectively.

It may be noted that an earlier version of HSE06, called HSE03 [274], has been available for the evaluation bandgaps. HSE03 is similar to HSE06 except parameter ω such that $\omega_{HF} = \omega_{PBE}$. Krukau et al. [275] showed that HSE06 introduces more error than HSE03 in calculating the bandgap and the deviation between between the two functionals decreases by decreasing the value of ω used in HSE06 calculations. Moreover, Heyd et al. [277] used HSE03 to calculate the bandgap of 40 semiconductor and insulator materials and found the mean absolute error to be 0.26 eV. However, the method tends to greatly underestimate solids with large bandgaps. The

calculated energy band structures with the GGA-PBE functional and the partial and total density of states for β- and δ-Ta_2O_5 with both GGA-PBE and PBE0 are shown in Figs. 17, 18, and 19 respectively [269].

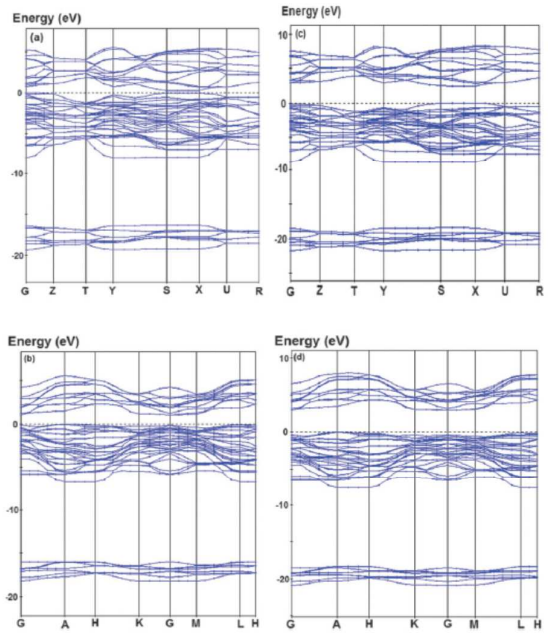

Fig. 17 Electronic band structure of (a) β-Ta_2O_5 under GGA-PBE calculation, (b) δ -Ta_2O_5 under GGA-PBE calculation, (c) β -Ta_2O_5 under PBE0 calculation, and (d) δ -Ta_2O_5 under PBE0 calculation [269]

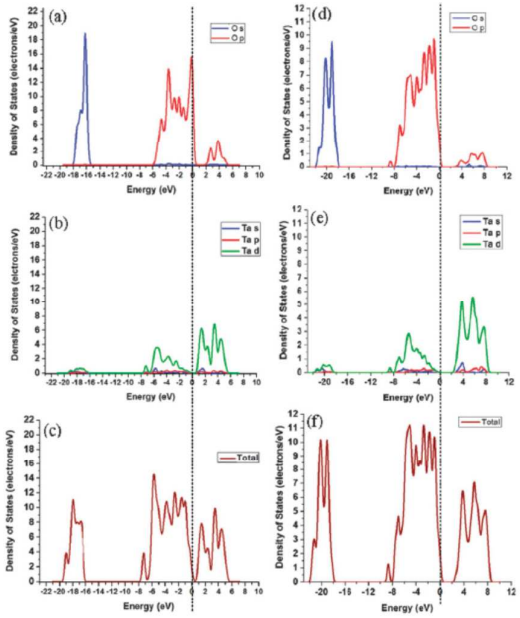

Fig. 18 Partial density of states in β -Ta2O5 of (a, d) O atoms; (b, e) Ta atoms; (c, f) total density of states of β -Ta2O5. (a)–(c) Uses GGA-PBE calculation and (d)–(f) uses PBE0 calculation [269]

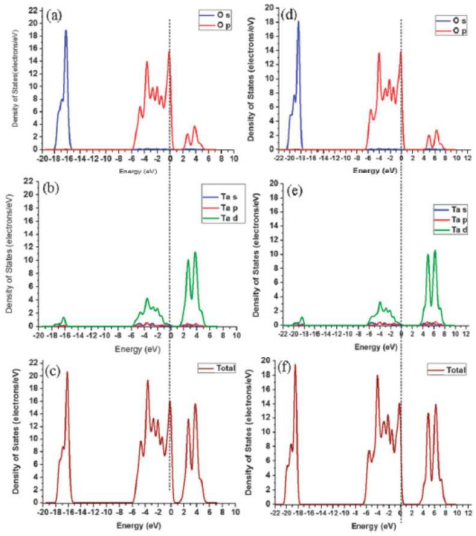

Fig. 19 Partial density of states in δ -Ta_2O_5 of (a, d) O atoms; (b, e) Ta atoms; (c, f) total density of states of δ -Ta_2O_5. (a)–(c) Uses GGA-PBE calculation and (d)–(f) uses PBE0 calculation [269].

Fig. 17 shows the obtained energy band structures of β- and δ-Ta_2O_5 with both GGA-PBE calculations. The β-phase has a direct bandgap of 0.2 eV whereas the δ-phase has an indirect bandgap of 1.04 eV, which occurs between the A-point and the Γ-point. Fig. 18 and 19 show the partial and total density of states of β- and δ-Ta_2O_5 respectively. The PDOS of Ta is quite different in the conduction band whereas the valence band is attributed by O 2p orbitals for both phases, which is the main cause for different bandgaps between two phases. Moreover, it is clear that both calculations with GGA-PBE and PBE0 are similar with the conduction band shifted to the right in the case of PBE0 to signify an increase in the band gap. The author of this paper concluded that GGA-PBE is good enough for qualitative analysis whereas quantitatively PBE0 results are correct. Similarly, Kweon et al. [87] performed hybrid functional calculations to study the structural, bonding and electronic properties of ms-$BiVO_4$ and ts-$BiVO_4$ using PBE and

PBE-HF hybrid functionals with varying HF exchange fractions (10%, 25% and 50%) and their calculated results revealed that an increase in the amount of HF exchange leads to an enhancement of the antibonding interaction between between Bi 6s and O 2p states, predicting energetically favored ms-$BiVO_4$ over ts-$BiVO_4$ when the HF fraction is greater than 25%. Wang et al. [117] studied structural and electronic properties of all phases of WO_3 using various hybrid functionals with both plane wave and localized basis sets and found that the HSE06 functional in combination with a plane wave basis set describes well the band gap of WO_3, whereas the B3LYP functional associated with a localized set slightly overestimates it. Rollmann et al. [32] have performed DFT + U calculations to account for the strong on-site Coulomb interaction present in α-Fe_2O_3 and found that with increasing U, the size of the band gap and magnetic moments increase and the best value for U = 4 eV was found to change the character of the gap from d-d to O-p-Fe-d. Fang et al. [57] used DFT-GGA aaproach to calculate the bandgaps of and found to be 1.8 eV and 1.1 eV respectively. These are not in consistent with experimental values reported. In order to get the better bandgaps, Herb et al. [252] have performed DFT calculations with the screened non-local hybrid HSE06 functional for tuning the photocatalytic properties of TaON and Ta_3N_5.

The DFT functionals play key role to investigate the eefect of doping on the band structure of photoanodes in water splitting. For example, Yin et al. [278] studied the codoping of TiO_2 to investigate the effect of doping on the band structure of metal oxide. They used DFT-GGA functional, which underestimated the bandgap. In order to calculate the more accurate bandgap value, the authors used hybrid functional HSE [279] with 22% of exact HF-exchange and found that CBM position agrees well whereas the VBM position is underestimated by 0.3 eV in the GGA calculations developed by Perdew and Wang [280]. Moreover, Yin et al. [281] studied monoclinic $BiVO_4$ using GGA functional and found the band gap of 2.06 eV, which is

underestimated by 0.44 eV. The authors considered doping of $BiVO_4$ with different groups namely I-A, II-A, II-B, and VI-B elemnts to optimize the electron and hole conductivities. They also considered substituting O with C or N or F and they concluded that their calculated results do not give good p- or n-conductivity due to strong compensation from intrinsic defects for substitutional alloying of O [281]. Moreover, Liu et al. [282] studied the photocatalytic properties of $Bi_{0.5}V_{0.5}VO_4$ (M = La, Eu, Sm, and Y). They found the bandgap of 2.58 eV for $Bi_{0.5}V_{0.5}VO_4$, which is smaller than bandgap of 2.82 eV for undoped $BiVO_4$. However, co-doping of Bi and Y resulted in an indirect bandgap. The fundamental direct bandgap for $Bi_{0.5}Y_{0.5}VO_4$ was 2.90 eV [282]. These results were higher than experimental value of 2.4-2.5 eV for pristine $BiVO_4$. In order to determine the origin of photocatalytic activity, Liu and co-workers considered different VO_4 compounds namely, $Bi_{0.5}Y_{0.5}VO_4$, $La_{0.5}Y_{0.5}VO_4$, and $Ce_{0.5}Y_{0.5}VO_4$ and found that only $Bi_{0.5}Y_{0.5}VO_4$ showed photocatalytic activity concluding that Bi ion and not VO_4 was responsible for enhancing the photocatalytic response [282]. Wang et al. [118] have studied the electronic properties of doped WO_3 using DFT calculations with hybrid functionals. They found that the top VB position is good for O_2 evolution in water splitting; however, the CB is too low for H_2 production and the band gap of WO_3 can be reduced to improve the activity with the visible light by doping of WO_3 with Mo or Cr due to the fact that doping can be used to alter the position of energy levels, thus resulting in a more efficient photocatalyst. They substituted W by Ti, Zr, or Hf ions and O by S in WO_3 to get the better photocatalytic activities. Pozun et al. [212] have presented a hybrid DFT study of doping effects in α-Fe_2O_3 and found that a screened hybrid functional with 12% exact exchange predicts a bandgap consistent with experimental result. They have also explored the case of increased doping of Pd into α-Fe_2O_3 and found correlation with previous experimental results. Nurlaela et al. [266] have performed DFT-HSE06 calculations for Ta_3N_5 based on partially oxidized $Ta_3N_{4.83}O_{0.17}$and N-deficient

$Ta_3N_{4.83}$ to calculate their electronic density of states and UV-Vis optical absorption spectra as shown Fig. 15 (i-iii) and found the better photocatalytic activities.

Consequently, DFT methods are very strong tools that can provide a systematic approach towards the design of photoanode materials. DFT is preferred over ab-initio methods due to its considerably reduced computational cost as it is based on calculating electron density instead of the wave function. The different functionals have been reported to investigate the best candidate for photoanode in photoelectrochemical cell. LDA- and GGA-based functionals tend to underestimate the bandgap in DFT calculations and excitation energy in TD-DFT calculations, influencing photocatalytic activities of the photoanode materials. Thus, hybrid functionals seem to give very accurate results for such systems, reducing the discrepancybetween theoretical calculations and experiments to only 5%, provided the right functional is chosen. In this regard, DFT can be considered as a fast computational screening method, with respect to stability and bandgap, to explore new light harvesting materials for water splitting.

5. Summary and Outlook

In summary, we have reviewed the structures and properties of $BiVO_4$, WO_3, α-Fe_2O_3, TaON, and Ta_3N_5 theoretically for their use as photoanode materials in photoelectrochemical cells and discussed various theoretical strategies that have been employed to characterize their photoelctrochemical properties. For oxides such as $BiVO_4$, WO_3, and α-Fe_2O_3, they are composed of inexpensive elements with the VB edge located over 1.23 V vs. NHE, providing sufficient overpotential for holes to photooxidize water while the CB edge is located at a bit more positive than the thermodynamic level for H_2, indicating the requirement of external bias voltage for H_2 evolution. Although, the band gaps of $BiVO_4$, WO_3, and α-Fe_2O_3 are slightly larger than is desired for a photoanode (ca. 2.0 eV), the CB position may compensate for their

disadvantage for efficiently utilizing visible light. In case of TaON and Ta_3N_5, they are potential candidates for solar water splitting due to their narrow band gap that allows visible light absorption and the sufficient negative level of CB for H_2 evolution. The CB edges of the oxynitrides consist predominantly of empty metal orbitals, resulting in similar high energy levels to those of corresponding metal oxides ($BiVO_4$, WO_3, α-Fe_2O_3). However, VB of oxynitrides are more negatrive than those of oxides due to the hybridization of N 2p and O 2p orbitals. Therefore, oxynitride materials possess appropriate band levels for visible-light-driven water splitting. The same phenomenon happens in case of nitride materials. In particular, TaON and Ta_3N_5 exhibit exciting water oxidation quantum yields of 34% and 10% with the ability to collect nearly 45% of the solar spectrum [268, 283], which confirms their high efficiency under visible light irradiation without assistance compared to oxides [284]. Consequently, oxynitrides, nitrides and even sulfides photocatalysts should be further improved to achieve higher quantum efficiencies.

To develop more efficient photoanode materials, it is necessary to narrow the band gap to harvest the visible light in the lower wavelength regions and enhance the photogenrated charge separation in photocatalysis. Thus, all of the factors such as crystallatinity, surface properties, morphology, chemical composition, structure and electronic properties will determine the photocatalytic activity of such materials. Currently, the available efficiency for overall water splitting systems for simultaneous H_2 and O_2 evolution under visible-light irradiation is still low due to fast charge recombination and backward reactions. Although, there are many impressive results, innovations and developments in new photonaode materials, structures and conceptions are still welcome. We strongly believe that this theoretical review article will provide some inspirations to researchers working in the field of PEC to design and develop new potential photoanode materials for solar water splitting with

higher efficiencies. Although, this review clearly shows that while a significant improvement in the development of above mentioned photoanode materials to date, there is still considerable room for further improvement.

DFT methods are very strong tools that can provide a systematic approach towards the design of photoanode materials. DFT is preferred over ab-initio methods due to its considerably reduced computational cost as it is based on calculating electron density instead of the wave function. The different functionals have been reported to investigate the best candidate for photoanode in photoelectrochemical cell. LDA- and GGA-based functionals tend to underestimate the bandgap in DFT calculations and excitation energy in TD-DFT calculations, influencing photocatalytic activities of the photoanode materials. In this regard, hybrid functionals seem to give very accurate results for such systems, reducing the discrepancybetween theoretical calculations and experiments to only 5%, provided the right functional is chosen. In order to able to select the right functional for the system, one should look closely at the expression of the exchange-correlation energy of the functional and have a rough understanding about the correlation between the electrons in the system under study. In this regard, DFT can be considered as a fast computational screening method, with respect to stability and bandgap, to explore new light harvesting materials for water splitting. Some examples of other materials for water splitting beyond the materials discussed already are as follows: Gan et al. [285] claimed that oxygen vacancies promote photoelectrochemical performance of In_2O_3 nanocubes bu using experimental techniques. Zhao et al. [286] investigated experimentally the single-layer or multi-layer molybdenum disulfide nanorose cross-linked by three-dimensional-reduced graphene oxide (MoS_2-NR/rGO) for superior water splitting. Liu et al. [287] designed and fabricated psuedobrookite Fe_2TiO_5 ultrathin layers grown on vertically aligned TiO_2 nanotube arrays that can enhance the conduction and utilization of

photogenerated charge carriers. Brillet et al. [288] introduced the concept of dual absorber tandem cell for highly efficient water-splitting. The authors considered a device based on an oxide photoanode and a dye-sensitized solar cell, which performed unassisted water splitting with an efficiency of up to 3.1% STH. Symes et al. [289] introduced an electron coupled proton buffer layer polyoxometalate ($H_3PMo_{12}O_{40}$) for decoupling hydrogen and oxygen evolution during electrolytic water splitting.

Acknowledgement

This work was supported by the Korea Center for Artificial Photosynthesis (KCAP, 2009-0093880, 2009-0093886), Basic Science Research Program (No. 2012-017247), BK Plus Program and A3 Foresight Program, all funded by the Ministry of Science, ICT and Future Planning through the National Research Foundation (NRF) Korea.

References

1. M. Gratzel, Nature, 2001, 414, 338.
2. N. S. Lewis and D. G. Nocera, Proc. Natl. Acad. Sci. USA, 2006, 103, 15729.
3. J. Z. Zhang, MRS Bull., 2011, 36, 48.
4. M. W. Kanan and D. G. Nocera, Science, 2008, 321, 1072.
5. U. A. Joshi, A. Palasyuk, D. Arney and P. A. Maggard, J. Phys. Chem. Lett., 2010, 1, 2719.
6. T. L. Thompson and J. T. Yates, Chem. Rev., 2006, 106, 4428.
7. N. J. Serpone, J. Phys. Chem. B, 2006, 110, 24287.
8. H. Zhang, G. Chen, D. W. Bahnemann, J. Mater. Chem. 2009, 19, 5085.
9. B. Xie, H. Zhang, P. Cai, R. Qiu and Y. Xiong, Chemosphere, 2006, 63, 956.
10. M. G. Walter, E. L. Warren, J. R. McKone, S. W. Boettcher, Q. Mi, E. A. Santori and N. S. Lewis, Chem. Rev., 2010, 110, 6446.
11. T. Bak, J. Nowotny, M. Rekas and C. C. Sorrell, Int. J. Hydrogen Energy, 2002, 27, 991.
12. M. N. Huda, Y. Yan, C. Y. Moon, S. H. Wei, M. M. Al-Jassim, Phys. Rev. B, 2008, 77, 195102.
13. R. Chatten, A. V. Chadwick, A. Rougier and P. J. D. Lindan, J. Phys. Chem. B, 2005, 109, 3146.
14. G. A. de Wijs, P. K. de Boer, R. A. de Groot and G. Kresse, Phys. Rev. B, 1999, 59, 2684.
15. F. Cora, M. G. Stachiotti, C. R. A. Catlow and C. O. Rodriguez, J. Phys. Chem. B, 1997, 101, 3945.
16. M. N. Huda, Y. Yan, S. H. Wei and M. M. Al-Jassim, Phys. Rev. B, 2009, 80, 115118.
17. F. Cora, A. Patel, N. M. Harrison, R. Dovesi, C. Richard and A. Catlow, J. Am. Chem. Soc., 1996, 118, 12174.
18. B. Ingham, S. C. Hendy, S. V. Chong and J. L. Tallon, Phys. Rev. B, 2005, 72, 075109.
19. A. Hjelm, C. G. Granqvist and J. M. Wills, Phys. Rev. B, 1996, 54, 2436.

20. D. B. Migas, V. L. Shaposhnikov, V. N. Rodin and V. E. Borisenko, J. Appl. Phys., 2010, 108, 093713.
21. S. K. Deb, Sol. Energy Mater. Sol. Cells, 2008, 92, 245.
22. S. K. Deb, Appl. Opt., 1969, 3, 192.
23. S. K. Deb, Philos. Mater., 1973, 27, 801.
24. J. M. Berek and J. J. Sienko, J. Solid State Chem., 1970, 2, 109.
25. M. A. Butler, R. D. Nasby and R. K. Quinn, Solid State Commun., 1976, 19, 1011.
26. D. E. Scaife, Sol. Energy, 1980, 25, 41.
27. A. Kudo and Y. Miseki, Chem. Soc. Rev., 2009, 38, 253.
28. A. J. Nozik, Annu. Rev. Phys. Chem., 1978, 29, 189.
29. L. Weinhardt, M. Blum, M. Bar, C. Heske, B. Cole, B. Marsen and E. L. Miller, J. Phys. Chem. C, 2008, 112, 3078.
30. M. N. Huda, Y. Walsh, Y. Yan, S. H. Wei and M. N. Al-Jassim, J. Appl. Phys., 2010, 107, 123712.
31. A. Rohrbach, J. Hafner and G. Kresse, Phys. Rev. B, 2004, 70, 125426.
32. G. Rollmann, A. Rohrbach, P. Entel and J. Hafner, Phys. Rev. B, 2004, 69, 165107.
33. A. Bandopadhyay, J. Velev, W. H. Butler, S. K. Sarker and O. Bengone, Phys. Rev. B, 2004, 69, 174429.
34. J. Lee and S. Han, Phys. Chem. Chem. Phys., 2013, 15, 18906.
35. R. Rivera, H. P. Pinto, A. Stashans and L. Piedra, Phys. Scr., 2012, 85, 015602.
36. X. Y. Meng, G. W. Qin, S. Li, X. H. Wen, Y. P. Ren, W. L. Pei and L. Zuo, Appl. Phys. Lett., 2011, 98, 112104.
37. P. Liao, M. C. Toroker and E. A. Carter, Nano Lett., 2011, 11, 1775.
38. D. M. Sherman and S. R. Randall, Geochim. Cosmochim. Acta, 2003, 67, 4223.

39. M. Blanchard, G. Morin, M. Lazzeri, E. Balan and I. Dabo, Geochim. Cosmochim. Acta, 2012, 86, 182.
40. S. Yin and D. E. Ellis, Surf. Sci., 2009, 603, 736.
41. K. D. Kwon and J. D. Kubicki, Langmuir, 2004, 20, 9249.
42. P. Persson, N. Nilsson and S. Sjoberg, J. Colloid Interface Sci., 1996, 177, 263.
43. Y. Arai and D. L. Sparks, J. Colloid Interface Sci., 2001, 241, 317.
44. J. D. Kubicki, K. D. Kwon, K. W. Paul and D. L. Sparks, Eur. J. Soil Sci., 2007, 58, 932.
45. N. Y. Acelas, S. M. Mejia, F. Mondragon and E. Florez, Comput. Theor. Chem., 2013, 1005, 16.
46. P. R. Grossl and D. L. Sparks, Geoderma, 1995, 67, 87.
47. P. R. Grossl, M. Eick and D. L. Sparks, Environ Sci. Technol., 1997, 31, 321.
48. J. G. Catalano, Z. Zhang, P. Fenter and M. J. Bedzyk, J. Colloid Interface Sci., 2006, 297, 665.
49. S. E. Mason, T. P. Trainor and C. J. Goffinet, Comput. Theor. Chem., 2012, 987, 103.
50. M. G. Walter, E. L. Warren, J. R. McKone, S. W. Boettcher, Q. Mi, E. A. Santori and N. S. Lewis, Chem. Rev., 2010, 110, 6446.
51. K. Maeda and K. Domen, J. Phys. Chem. C, 2007, 111, 7851.
52. S. Wang and L. W. Wang, Phys. Rev. Lett., 2010, 104, 065501.
53. K. Maeda, M. Higashi, D. Lu, R. Abe and K. Domen, J. Am. Chem. Soc., 2010, 132, 5858.
54. K. Maeda, R. Abe and K. Domen, J. Phys. Chem. C, 2011, 115, 3057.
55. R. Abe, M. Higashi and K. Domen, J. Am. Chem. Soc., 2010, 132, 11828.
56. M. Yashima, Y. Lee and K. Domen, Chem. Mater., 2007, 19, 588.
57. C. M. Fang, E. Orhan, G. A. de Wijs, H. T. Hintzen, R. A. de Groot, R. Marchand, J. Y. Saillard and G. de With, J. Mater. Chem., 2001, 11, 1248.

58. C. Stampfl and A. J. Freeman, Phys. Rev. B: Condens. Matter Mater. Phys., 2003, 67, 064108.
59. C. Stampfl and A. J. Freeman, Phys. Rev. B: Condens. Matter Mater. Phys., 2005, 71, 024111.
60. P. Li, W. Fan, Y. Li, H. Sun, X. Cheng, X. Zhao and M. Jiang, Inorg. Chem., 2010, 49, 6917.
61. J. Gan, X. Lu and Y. Tong, Nanoscale, 2014, 6, 7142.
62. J. A. Turner, Science, 1999, 285, 1493.
63. J. R. Bolton, S. J. Strickler and J. S. Connolly, Nature, 1985, 316, 495.
64. M. F. Weber and M. J. Dignam, J. Electrochem. Soc., 1984, 131, 1258.
65. A. Walsh, Y. Yan, M. N. Huda, M. M. Al-Jassim and S. Wei, Chem. Mater., 2009, 21, 547.
66. A. Kudo, K. Omori and H. Kato, J. Am. Chem. Soc., 1999, 121, 11459.
67. H. Luo, H. Mueller, T. M. McCleskey, A. K. Burrell, E. Bauer and Q. X. Jia, J. Phys. Chem. C, 2008, 112, 6099.
68. K. Sayama, A. Nomura, T. Arai, T. Sugita, R. Abe, M. Yanagida, T. Oi, Y. Iwasaki, Y. Abe and H. Sugihara, J. Phys. Chem. B, 2006, 110, 11352.
69. H. S. Park, K. E. Kweon, H. Ye, E. Paek, G. S. Hwang and A. J. Bard, J. Phys. Chem. C, 2011, 115, 17870.
70. H. Ye, J. Lee, J. S. Jang, and A. J. Bard, J. Phys. Chem. C, 2010, 114, 13322.
71. S. Tokunaga, H. Kato and A. Kudo, Chem. Mater., 2001, 13, 4624.
72. J. Yu and A. Kudo, Adv. Funct. Mater., 2006, 16, 2163.
73. J. D. Bierlein and A. W. Sleight, Solid State Commun., 1975, 16, 69.
74. M. Oshikiri, M. Boero, J. Ye, Z. Zou and G. Kido, J. Chem. Phys., 2002, 117, 7313.
75. M. W. Stoltzfus, P. M. Woodword, R. Seshadri, J. H. Klepeis and B. Bursten, Inorg. Chem., 2007, 46, 3839.

76. M. Oshikiri and M. Boero, J. Phys. Chem. B, 2006, 110, 9188.

77. M. Oshikiri, M. Boero, A. Matsushita and J. Ye, J. Electrochem., 2009, 22, 114.

78. A. Kudo, K. Ueda, H. Kato and I. Mikami, Catal. Lett., 1998, 53, 229.

79. S. Kohtani, M. Koshiko, A. Kudo, K. Tokumura, Y. Ishigaki, A. Toriba, K. Hayakawa and R. Nagasaki, Appl. Catal. B, 2003, 46, 573.

80. S. Kohtani, J. Hiro, N. Yamamoto, A. Kudo, K. Tokumura and R. Nagasaki, Catal. Commun., 2005, 6, 185.

81. K. Sayama, A. Nomura, Z. Zou, R. Abe, Y. Abe and H. Arakawa, Chem. Commun., 2003, 2908.

82. X. Zhang, Z. Ai, F. Jia, L. Zhang, X. Fan and Z. Zou, Mater. Chem. Phys., 2007, 103, 162.

83. M. Oshikiri and M. Boero, J. Phys. Chem. B, 2006, 110, 9188.

84. R. Car and M. Parrinnelo, Phys. Rev. Lett., 1985, 55, 2471.

85. H. S. Park, K. E. Kweon, H. Ye, E. Pack, G. S. Hwang and A. J. Bard, J. Phys. Chem. C, 2011, 115, 17870.

86. Z. Zhao, Z. Li and Z. Zou, Phys. Chem. Chem. Phys., 2011, 13, 4746-4753.

87. K. E. Kweon and G. S. Hwang, Phys. Rev. B, 2012, 86, 165209.

88. G. Wang, Y. Ling, X. Lu, F. Qian, Y. Tong, J. Z. Zhang, V. Lordi, C. R. Leao and Y. Li, J. Phys. Chem. C, 2013, 117, 10957.

89. J. K. Cooper, S. Gul, F. M. Toma, L. Chen, P-A. Glans, J. Guo, J. W. Ager, J. Yano and I. D. Sharp, Chem. Mater., 2014, 26, 5365.

90. J. Ma and L. W. Wang, Appl. Phys. Lett., 2014, 105, 172102.

91. D. J. Payne, R. J. Egdell, A. Walsh, G. W. Watson, J. H. Guo, P. A. Glans, T. Learmonth and K. E. Smith, Phys. Rev. Lett. 2006, 96, 157403.

92. A. Walsh, G. W. Watson, D. J. Payne, R. J. Egdell, J. H. Guo, P. A. Glans, T. Learmonth

and K. E. Smith, Phys. Rev. B, 2006, 73, 235104.

93. A. Walsh and G. W. Watson, Chem. Mater., 2007, 19, 5158.
94. A. Walsh, G. W. Watson, D. J. Payne, G. Atkinson and R. J. Egdell, J. Mater. Chem., 2006, 16, 3452.
95. Y. Park, K. J. McDonald and K. S. Choi, Chem. Soc. Rev., 2013, 42, 2321.
96. W. L. Kehl, R. G. Hay and D. J. Wahl, J. Appl. Phys., 1952, 23, 212.
97. J. Wyart and M. C. R. Foex, Acad. Sci., 1951, 233, 2459.
98. E. Salje, Acta Crystallogr. B, 1977, 33, 574.
99. B. O. Loopstra and P. Boldrini, Acta Crystallogr., 1966, 21, 158.
100. E. Salje and K. Viswanathan, Acta Crystallogr. B, 1975, 31, 356.
101. R. Diehl, G. Brandt and E. Salje, Acta Crystallogr. B, 1978, 34, 1105.
102. M. Ai, J. Catal., 1977, 49, 305.
103. T. Yamaguchi, Y. Tanaka and K. Tanabe, J. Catal., 1980, 65, 442.
104. L. Lietti, J. Svachula, P. Forzatti, G. Busca, G. Ramis and F. Bregani, Catal. Today, 1993, 17, 131.
105. M. J. Sienko, In Non-Stoichiometric Compounds; R. F. Gould, Ed; Advances in Chemistry Series; ACS: Washington, DC, 1963, P. G. Dickens and M. S. Q. Whittingham, Rev. Chem. Soc., 1968, 22, 30.
106. E. Salje, J. Appl. Crystallogr., 1974, 7, 615.
107. M. Sundberg and R. J. D. Tiley, J. Solid State Chem., 1974, 11, 150.
108. D. W. Bullett, J. Phys. C, 1983, 16, 2197.
109. D. W. Bullett, Solid State Commun., 1983, 46, 575.
110. C. G. Zhan and F. Zheng, J. Mol. Struct: THEOCHEM, 1993, 285, 89.
111. A. Stashans and S. Lunell, Int. J. Quantum. Chem., 1997, 63, 729.

112. T. Vogt, P. M. Woodward and B. A. Hunter, J. Solid State Chem., 1999, 144, 209.

113. P. M. Woodward, A. W. Sleight and T. Vogt, J. Solid State Chem., 1997, 131,9.

114. B. Gerand, G. Novogorocki, J. Guenot and M. Figlarz, J. Solid State Chem., 1979, 29, 429.

115. C. L. Mauriat and V. Oison, J. Phys: Condens. Matter., 2006, 18, 7361.

116. T. Pagnier and A. Pasturel, J. Phys: Condens. Matter., 2003, 15, 3121.

117. F. Wang, C. D. Valentin and G. Pacchioni, J. Phys. Chem. C, 2011, 115, 8345.

118. F. Wang, C. D. Valentin and G. Pacchioni, J. Phys. Chem. C, 2012, 116, 8901.

119. Y. Ping, Y. Li, F. Gygi and G. Galli, Chem. Mater., 2012, 24, 4252.

120. Y. Ping, Y. Li, D. Rocca and G. Galli, Phys. Rev. B, 2013, 87, 165203.

121. J. Kleperis, J. Zubkans and A. R. Lusis, Proc. SPIE, 1997, 2968, 186.

122. F. Koffyberg, K. Dwight and A. Wold, Solid State Commun., 1979, 30, 433.

123. Y. Ping and G. Galli, J. Phys. Chem. C, 2014, 118, 6019.

124. M. Green and Z. Hussain, J. Appl. Phys., 1991, 69, 7788.

125. J. Desilvestro and M. Gratzel, J. Electroanal. Chem., 1987, 238, 129.

126. D. Paluselli, B. Marsen, E. L. Miller and R. E. Rocheleau, Electrochem. Solid State Lett., 2005, 8, G301.

127. J. Tang and J. Ye, J. Mater. Chem., 2005, 15, 4246.

128. P. Maruthamuthu, M. Ashokkumar, K. Gurunathan, E. Subramanian and M. Sastri, Int. J. Hydrogen Energy, 1989, 14, 525.

129. Q. Mi, Y. Ping, Y. Li, B. Cao, B. S. Brunschwig, P. G. Khalifah, G. A. Galli, H. B. Gray and N. S. Lewis, J. Am. Chem. Soc., 2012, 134, 18318.

130. G. A. Prinz, Phys. Rev. Lett., 1985, 54, 1051.

131. S. Degroote, A. Vantomme, J. Dekoster and G. Langouche, Appl. Surf. Sci., 1995, 91,

72.

132. X. Yuxing, T. Qiangqiang, T. Zilong, Z. Zhongtai and Y. Zhangfu, Rare Metal Mater. Eng., 2010, 39, 753.

133. J. Zhou, Y. Ding, S. Deng, L. Gong, N. Xu and Z. Wang, Adv. Mater., 2005, 17, 2107.

134. W. Wu, Q. Yu, J. Lian, J. Bao, Z. Liu and S. S. Pei, J. Cryst. Growth, 2010, 312, 3147.

135. J. Guo, Y. Li, S. Zhu, Z. Chen, Q. Liu, D. Zhang, W. J. Moon and D. M. Song, RSC Adv., 2012, 2, 1356.

136. Q. Mi, A. Zhanaidarova, B. S. Brunschwig, H. B. Gray and N. S. Lewis, Energy Environ. Sci., 2012, 5, 5694.

137. N. T. Hahn, H. Ye, D. W. Flaherty, A. J. Bard and C. B. Mullins, ACS Nano, 2010, 4, 1977.

138. R. M. Cornell and U. Schwertmann, Iron Oxides in the Laboratory: Preparation and Characterization, 2nd ed.; Wiley-VCH: New York, NY, USA, 2000.

139. R. M. Cornell and U. Schwertmann, The Iron Oxides: Structure, Properties, Reactions, Occurences, and Uses, 2nd ed.; Wiley-VCH: New York, NY, USA, 2003.

140. C. Wu, P. Yin, X. Zhu, C. OuYang and Y. Xie, J. Phys. Chem. B, 2006, 110, 17806.

141. S. Zeng, K. Tang, T. Li, Z. Liang, D.Wang, Y.Wang and W. Zhou, J. Phys. Chem. C, 2007, 111, 10217.

142. Z. Wu, K. Yu, S. Zhang and Y. Xie, J. Phys. Chem. C, 2008, 112, 11307.

143. W. S. Choi, H. Y. Koo, Z. Zhongbin, Y. Li and D.-Y. Kim, Adv. Funct. Mater., 2007, 17, 1743.

144. X. Gou, G.Wang, J. Park, H. Liu and J. Yang, Nanotechnology, 2008, 19, 125606.

145. E. Liger, L. Charlet and P. van Cappellen, Geochim. Cosmochim. Acta, 1999, 63, 2939.

146. F. Herrera, A. Lopez, G. Mascolo, P. Albers and J. Kiwi, Applied Catalysis B: Environmental, 2001, 29, 147.

147. H. H. Huang, M.-C. Lu and J.-N. Chen, Water Res., 2001, 35, 2291.

148. O. Shekhah, W. Ranke, A. Schüle, G. Kolios and R. Schlögl, Angew. Chem., Int. Ed., 2003, 42, 5760.

149. P. Li, D. E.Miser, S. Rabiei, R. T. Yadav and M. R. Hajaligol, Appl. Catal. B, 2003, 43, 151.

150. R. Mecozzi, L. di Palma, D. Pilone and L. Cerboni, J. Hazard. Mater. B, 2006, 137, 886.

151. P. R. Christensen, R. V. Morris, M. D. Lane, J. L. Bandfield and M. C. Malin, J. Geophys. Res., 2001, 106, 23873.

152. D. C. Catling and J. M. Moore, Icarus, 2003, 165, 277.

153. I. Fleischer, D. G. Agresti, G. Klingelhöfer and R. V. Morris, J. Geophys. Res., 2010, 115, E00F06.

154. A. S. Madden, V. E. Hamilton, M. E. E. Madden, P. R. Larson and M. A. Miller, Earth Planet. Sci. Lett., 2010, 298, 377.

155. A. Johnson, L. Pratt, T. Vishnivetskaya, S. Pfiffner, R. Bryan, E. Dadachova, L. Whyte, K. Radtke, E. Chan, S. Tronick, G. Borgonie, R. Mancinelli, L. Rothschild, D. Rogoff, D. Horikawa and T. Onstott, Icarus, 2011, 211, 1162.

156. N. Beermann, L. Vayssieres, S.-E. Lindquist, and A. Hagfeldt, J. Electrochem. Soc., 2000, 147, 2456.

157. G. K. Mor, H. E. Prakasam, O. K. Varghese, K. Shankar and C. A. Grimes, Nano. Lett., 2007, 7, 2356.

158. T. Lopes, L. Andrade, H. A. Ribeiro and A. Mendes, Int. J. Hydrogen Energy, 2010, 35, 11601.

159. L. Pauling and S. B. Hendricks, J. Am. Chem. Soc., 1925, 47, 781.

160. C. W. Searle and G. W. Dean, Phys. Rev. B, 1970, 1, 4337.

161. L. M. Levinson, Phys. Rev. B, 1971, 3, 3965.

162. Y. Sato and S. Akimoto, J. Appl. Phys., 1979, 50, 5285.

163. L. W. Finger and R. M. Hazen, J. Appl. Phys., 1980, 51, 5362.

164. T. Yagi and S. Akimoto, High Pressure Research in Geophysics ,Kluwer Academic, Tokyo, 1982.

165. T. Suzuki, T. Yagi, A. Akimoto, A. Ito, S. Morimoto and S. Syono, Solid State Physics Under Pressure, KTK Scientific, Tokyo, 1985.

166. A. Fujimori, M. Saeki, N. Kimizuka, M. Taniguchi and S. Suga, Phys. Rev. B, 1989, 34, 7318.

167. R. J. Lad and V. E. Henrich, Phys. Rev. B, 1989, 39, 13478.

168. F. Ciccacci, L. Braicovich, E. Puppin and E. Vescovo, Phys. Rev. B, 1991, 44, 10444.

169. J. S. Olsen, C. S. G. Cousins, L. Gerward, H. Jhans and B. J. Sheldon, Phys. Scr., 1991, 43, 327.

170. G. Drager, W. Czolbe and J. A. Leiro, Phys. Rev. B, 1992, 45, 8283.

171. D. L. A. de Faria, S. V. Silva and M. T. de Oliveira, J. Raman Spectrosc., 1997, 28, 873.

172. T. Uozumi, K. Okada, A. Kotani, R. Zimmermann, P. Steiner, S. Hufner, Y. Tezuka and S. Shin, J. Electron Spectrosc. Relat. Phenom., 1997, 83, 9.

173. M. Z. Dang, D. G. Rancourt, J. E. Dutrizac, G. Lamarche and R. Provencher, Hyperfine Interact., 1998, 117, 271.

174. J. Badro, V. V. Struzhkin, J. Shu, R.J. Hemley, H. K. Mao, C. C. Kao, J. P. Rueff and G. Shen, Phys. Rev. Lett., 1999, 83, 4101.

175. M. P. Pasternak, G. K. Rozenberg, G. Y. Machavariani, O. Naaman, R. D. Taylor and R. Jeanloz, Phys. Rev. Lett., 1999, 82, 4663.

176. G. K. Rozenberg, L. S. Dubrovinsky, M. P. Pasternak, O. Naaman, T. LeBihan and R.

Ahuja, Phys. Rev. B, 2002, 65, 064112.

177. J. Badro, G. Fiquet, V. V. Struzhkin, M. Somayazulu, H. K. Mao, G. Shen and T. LeBihan, Phys. Rev. Lett., 2002, 89, 205504.

178. K. Lefmann, F. Bo.dker, M.F. Hansen, H. Vazquez, N.B. Christensen, P. A. Lindgard, K.N. Clausen and S. Mo. rup, Eur. Phys. J. D, 1999, 9, 491.

179. F. Bodker, M. F. Hansen, C. B. Koch, K. Lefmann and S. Mo. rup, Phys. Rev. B, 2000, 61, 6826.

180. F. J. Morin, Phys. Rev., 1950, 78, 819.

181. M. D. Towler, N. L. Allan, N. M. Harrison, V. R. Saunders, W. C. Mackrodt and E. Apra`, Phys. Rev. B, 1994, 50, 5041.

182. Z. Fang, I. V. Solovyev, H. Sawada and K. Terakura, Phys. Rev. B, 1999, 59, 762.

183. O. Bengone, M. Alouani, P. Blochl and J. Hugel, Phys. Rev. B, 2000, 62, 16392.

184. S. L. Dudarev, G. A. Botton, S. Y. Savrasov, C. J. Humphreys and A. P. Sutton, Phys. Rev. B, 1998, 57, 1505.

185. M. R. Castell, S. L. Dudarev, G. A. D. Briggs and A. P. Sutton, Phys. Rev. B, 1999, 59, 7342.

186. D. Kodderitzsch, W. Hergert, W. M. Temmerman, Z. Szotek, A. Ernst and H. Winter, Phys. Rev. B, 2002, 66, 064434.

187. G. Pacchioni, Surf. Rev. Lett., 2000, 7, 277.

188. M. Catti, G. Valerio and R. Dovesi, Phys. Rev. B, 1995, 51, 7441.

189. L. M. Sandratskii, M. Uhl, and J. Kubler, J. Phys.: Condens. Matter, 1996, 8, 983.

190. M. P. J. Punkkinen, K. Kokko, W. Hergert and I. J. Vayrynen, J. Phys.: Condens. Matter, 1999, 11, 2341.

191. H. Chow and F. Keffer, Phys. Rev. B, 1974, 10, 243.

192. L. M. Sandratskii and J. Kubler, Europhys. Lett., 1996, 33, 447.

193. K. Sivula, F. Le Formal and M. Grätzel, ChemSusChem, 2011, 4, 432.

194. S. C. Warren, K. Voitchovsky, H. Dotan, C. M. Leroy, M. Cornuz, F. Stellacci, C. Hebert, A. Rotschild and M. Grätzel, Nat. Mater., 2013, 12, 842.

195. A. Kay, I. Cesar and M. Grätzel, J. Am. Chem. Soc., 2006, 128, 15714.

196. S. D. Tilley, M. Cornuz, K. Sivula and M. Grätzel, Angew. Chem., Int. Ed., 2010, 49, 6405.

197. C. M. Eggleston and M. F. Hochella, Jr., Am. Miner., 1992, 77, 911.

198. C. M. Eggleston and W. Stumm, Geochim. Cosmochim. Acta, 1993, 57, 4843.

199. J. L. Junta-Rosso and M. F. Hochella, Jr., Geochim. Cosmochim. Acta, 1996, 60, 305.

200. T. P. Trainor, A. M. Chaka, P. J. Eng, M. Newville, G. A. Waychunas, J. G. Catalano and G. E. Brown, Jr., Surf. Sci., 2004, 573, 204.

201. M. Lübbe and W. Moritz, J. Phys.: Condens. Matter, 2009, 21, 134010.

202. S. Yamamoto, T. Kendelewicz, J. T. Newberg, G. Ketteler, D. E. Starr, E. R. Mysak, K. J. Andersson, H. Ogasawara, H. Bluhm, M. Salmeron, G. E. Brown, Jr. and A. Nilsson, J. Phys. Chem. C, 2010, 114, 2256.

203. C. Lemire, S. Bertarione, A. Zecchina, D. Scarano, A. Chaka, S. Shaikhutdinov and H. J. Freund, Phys. Rev. Lett., 2005, 94, 166101.

204. A. Barbier, A. Stierle, N. Kasper, M. J. Guittet and J. Jupille, Phys. Rev. B, 2007, 75, 233406.

205. J. Rossmeisl, Z. W. Qu, H. Zhu, G. J. Kroes and J. K. Nørskov, J. Electroanal. Chem., 2007, 607, 83.

206. J. K. Nørskov, J. Rossmeisl, A. Logadottir, L. Lindqvist, J. R. Kitchin, T. Bligaard and H. Jónsson, J. Phys. Chem. B, 2004, 108, 17886.

207. Á. Valdés, Z. W. Qu, G. J. Kroes, J. Rossmeisl and J. K. Nørskov, J. Phys. Chem. C, 2008, 112, 9872.

208. Á. Valdés and G. J. Kroes, J. Chem. Phys., 2009, 130, 114701.

209. A. Hellman and R. G. S. Pala, J. Phys. Chem. C, 2011, 115, 12901.

210. P. Liao, J. A. Keith and E. A. Carter, J. Am. Chem. Soc., 2012, 134, 13296.

211. A. K. Schwarsctein, M. N. Huda, A. Walsh, Y. Yan, G. D. Stucky, Y. S. Hu, M. M. Al-Jassim, E. W. McFarland, Chem. Mater., 2010, 22, 510.

212. Z. D. Pozun and G. Henkelman, J. Chem. Phys., 2011, 134, 224706.

213. X. Meng, G. Qin, W. A. Goddard III, S. Li, H. Pan, X. Wen, Y. Qin and L. Zuo, J. Phys. Chem. C, 2013, 117, 3779.

214. A. Fujimori, M. Saeki, M. Kimizuka, M. Taniguchi and S. Suga, Phys. Rev. B, 1986, 34, 7318.

215. T. Liu, L. Xue, X. Guo and C. G. Zheng, Fuel, 2014, 115, 179.

216. N. Y. Dzade, A. Roldan and N. H. de Leeuw, Minerals, 2014, 4, 89.

217. M. T. Nguyen, N. Seriani, S. Piccinin and R. Gebauer, J. Chem. Phys., 2014, 140, 064703.

218. J. K. Norskov, J. Rossmeisl, A. Logadottir, L. Lindqvist, J. R. Kitchin, T. Bligaard and H. Jonsson, J. Phys. Chem. B, 2004, 108, 17886.

219. N. Iordanova, M. Dupuis and K. M. Rosso, J. Chem. Phys., 2005, 122, 144305.

220. K. M. Rosso, D. M. A. Smith and M. J. Dupuis, J. Chem. Phys., 2003, 118, 6455.

221. J. Velev, A. Bandyopadhyay, W. H. Butler and S. Sarker, Phys. Rev. B, 2005, 71, 205208.

222. T. Droubay, K. M. Rosso, S. M. Heald, D. E. McCready, C. M. Wang and S. A. Chambers, Phys. Rev. B, 2007, 75, 104412.

223. M. Fukazawa, H. Matuzaki and K. Hara, J. Sens. Actuator B, 1993, 13, 521.

224. C. M. Eggleston, A. J. A. Shankle, A. J. Moyer, I. Cesar and M. Gratzel, Aquat. Sci., 2009, 71, 151.

225. S. Venkataraj, D. Severin, S. H. Mohamed, J. Ngaruiya, O. Kappertz and M. Wuttig, Thin Solid Films, 2006, 502, 228.

226. Y. I. Kim, P. M. Woodward, K. J. Baba-Kishi and C. W. Tai, Chem. Mater., 2004, 16, 1267.

227. K. Miga, K. Stanczyk, C. Sayag, D. Brodzki and G. Djega-Mariadassou, J. Catal., 1999, 183, 63.

228. G. Hitoki, T. Takata, J. N. Kondo, M. Hara, H. Kobayashi and K. Domen, Chem. Commun., 2002, 1698.

229. R. Nakamura, T. Tanaka and Y. Nakato, J. Phys. Chem. B, 2005, 109, 8920.

230. G. Brauer and J. Weidlein, Angew. Chem., 1965, 77, 913.

231. D. Armytage and B. E. F. Fender, Acta Crystallogr., Sect. B: Struct. Crystallogr. Cryst. Chem., 1974, 30, 809.

232. Y. A. Buslaev, G. M. Safronov, V. I. Pachomov, M. A. Glushkova, V. P. Repko, M. M. Ershova, A. N. Zhukov, T. A. Zhdanova, I. Akad and S. S. S. R. Nauk, Neorg. Mater., 1969, 5, 45.

233. M. W. Lumey and R. Dronskowski, Z. Anorg Allg. Chem., 2003, 629, 2173.

234. H. Schilling, A. Stork, E. Irran, H. Wolff, T. Bredow, R. Dronskowski, and M. Lerch, Angew Chem. Int. Ed., 2007, 46, 2931.

235. J. Wang, T. Fang, L. Zhang, J. Feng, Z. Li and Z. Zou, J. Catal., 2014, 309, 291.

236. J. Paier, M. Marsman, K. Hummer, G. Kresse, I. C. Gerber and J. G. Angyan, J. Chem. Phys., 2006, 124, 154709.

237. M. Harb, P. Sautet and P. Raybaud, J. Phys. Chem. C, 2011, 115, 19394.

238. M. Harb, P. Sautet and P. Raybaud, J. Phys. Chem. C, 2013, 117, 8892.

239. M. Harb, J. Phys. Chem. C, 2013, 117, 12942.

240. M. Harb, D. Masih, S. Ould-Chikh, P. Sautet, J. M. Basset and K. Takanabe, J. Phys. Chem. C, 2013, 117, 17477.

241. M. Harb, J. Phys. Chem. C, 2013, 117, 25229.

242. M. Hara, E. Chiba, A. Ishikawa, T. Takata, J. N. Kondo and K. J. Domen, J. Phys. Chem. B, 2003, 107, 13441.

243. M. Hara, G. Hitoki, T. Takata, J. N. Kondo, H. Kobayashi and K. Domen, Catl. Today, 2003, 78, 555.

244. W. J. Chun, A. Ishikawa, H. Fujisawa, T. Takata, J. N. Kondo, M. Hara, M. Kawai, Y. Matsumoto and K. Domen, J. Phys. Chem. B, 2003, 107, 1798.

245. E. Orhan, F. Tessier and R. Marchand, Solid State Sci., 2002, 4, 1071.

246. N. Al-Aqtash, F. Apostol, W. N. Mei and R. F. Sabirianov, J. Solid State Chem., 2013, 198, 337.

247. S. Chen and L. W. Wang, Appl. Phys. Lett., 2011, 99, 222103.

248. T. Chihi, M. Fatmi, M. Guemmaz and J. C. Parlebas, ISRN Metallurgy, 2012, 1.

249. L. Abbondanza and L. Meda, Energy Procedia, 2012, 22, 3.

250. Z. Wang, J. Hou, C. Yang, S. Jiao, K. Huang and H. Zhu, Energy Environ. Sci., 2013, 6, 2134.

251. A. Mukherji, R. Marschall, A. Tanksale, C. Sun, S. C. Smith, G. Q. Lu and L. Wang, Adv. Funct. Mater., 2011, 21, 126.

252. M. Harb, P. Sautet, E. Nurlaela, P. Raybaud, L. Cavallo, K. Domen, J. M. Basset and K. Takanabe, Phys. Chem. Chem. Phys., 2014, 16, 20548.

253. A. H. Reshak, Phys. Chem. Chem. Phys., 2014, 16, 10558.

254. A. M. Hafez, N. M. Salem and N. K. Allam, Phys. Chem. Chem. Phys., 2014, 16, 18418.

255. K. Takanabe and K. Domen, Green, 2011, 1, 313.

256. K. Maeda and K. Domen, J. Phys. Chem. Lett., 2010, 1, 2655.

257. Y. Lee, K. Nukumizu, T. Watanabe, T. Takata, M. Hara, M. Yoshimura and K. Domen, Chem. Lett., 2006, 35, 352.

258. R. Abe, J. Photochem. Photobiol. C, 2010, 11, 179.

259. S. J. Henderson and A. L. Hector, J. Solid State Chem., 2006, 179, 3518.

260. L. Yuliati, J. H. Yang, X. Wang, K. Maeda, T. Takata, M. Antonietti and K. Domen, J. Mater. Chem., 2010, 20, 4295.

261. C. T. Ho, K. B. Low, R. F. Klie, K. Maeda, K. Domen, R. J. Meyer and P. T. Snee, J. Phys. Chem. C, 2010, 115, 647.

262. Z. Chen, T. F. Jaramillo, T. G. Deutsch, A. Kleiman-Shwarsctein, A. J. Forman, N. Gaillard, R. Garland, K. Takanabe, C. Heske, M. Sunkara, E. W. McFarland, K. Domen, E. L. Miller, J. A. Turner and H. N. Dinh, J. Mater. Res., 2010, 25, 3.

263. Y. Li, T. Takata, D. Cha, K. Takanabe, T. Minegishi, J. Kubota and K. Domen, Adv. Mater., 2013, 25, 125.

264. A. Ishikawa, T. Takata, J. No. Kondo, M. Hara and K. Domen, J. Phys. Chem. B, 2004, 108, 11049.

265. M. Harb, L. Cavallo and J. M. Basset, J. Phys. Chem. C, 2014, 118, 20784.

266. E. Nurlaela, S. Ould-Chikh, M. Harb, S. del Gobbo, M. Aouine, E. Puzenat, P. Sautet, K. Domen, J. M. Basset and K. Takanabe, Chem. Mater., 2014, 26, 4812.

267. J. M. Morbec, I. Narkeviciute, T. F. Jaramillo and G. Galli, Phys. Rev. B, 2014, 90, 155204.

268. G. M. Wang, Y. C. Ling, H. Y. Wang, X. Y. Wang, C. C. Wang, J. Z. Zhang and Y. Li, Energy

Environ. Sci., 2012, 5, 6180.

269. R. Nashed, W. M. I. Hassan, Y. Ismail and N. K. Allam, Phys. Chem. Chem. Phys., 2013, 15, 1352.

270. K. M. Parida, S. K. Mahanta, S. Martha and A. Nashim, Int. J. Energy Res., 2011, 36, 12753.

271. M. Stodolny and M. Laniecki, Catal. Today, 2009, 142, 314.

272. W. J. Chun, A. Ishikawa, H. Fujisawa, T. Takata, J. N. Kondo, M. Hara, M. Kawai, Y. Matsumoto and K. Domen, J. Phys. Chem. B, 2003, 107, 1798.

273. A. V. Krukau, O. A. Vydrov, A. F. Izmaylov and G. E. Scuseria, J. Chem. Phys., 2006, 125, 224106.

274. J. Heyd and G, E, Scuseria, J. Chem. Phys., 2004, 120, 7274.

275. Y. N. Wu, L. Li and H. P. Cheng, Phys. Rev. B: Condens. Matter. Phys., 2011, 83, 144105.

276. J. Jaramillo, G. E. Scuseria and M. Ernzerhof, J. Chem. Phys., 2003, 118, 1068.

277. J. Heyd, J. E. Peralta, G. E. Scuseria and R. L. Martin, J. Chem. Phys., 2005, 123, 174101.

278. W. J. Yin, H. Tang, S. H. Wei, M. M. Al-Jassim, J. Turner and Y. Yan, Phys. Rev. B, 2010, 82, 045106.

279. J. Heyd, G. E. Scuseria and M. Ernzerhof, J. Chem. Phys., 2003, 118(18), 8207.

280. J. P. Perdew and Y. Wang, Phys. Rev. B, 1992, 45(23), 13244.

281. W. J. Yin, S. H. Wei, M. M. Al-Jassim, J. Turner and Y. F. Yan, Phys. Rev. B, 2011 83(15), 155102.

282. H. Liu, J. Yuan, Z. Jiang, W. F. Shangguan, H. Einaga and Y. Teraoka, J. Solid State Chem., 2012, 186, 70.

283. X. Y. Yang, A. Wolcott, G. M. Wang, A. Sobo, R. C. Fitzmorris, F. Qian, J. Z. Zhang and Y.

Li, Nano Lett., 2009, 9, 2331.

284. F. G. Wakim, Phys. Status Solidi A, 1970, 1, 479.

285. J. Gan, X. Lu, J. Wu, S. Xie, T. Zhai, M. Yu, Z. Zhang, Y. Mao, S. C. Wang, Y. Shen and Y. Tong, Scientif. Rep., 2013, 3, 1021.

286. Y. Zhao, L. Kuai, P. Wang, Y. Liu, P. Wang, H. Arandiyan, S. Cao, J. Zhang, F. Li, Q. Wang, B. Geng and H. Sun, Scientif. Rep., 2015, 5, 8722.

287. Q. Liu, J. He, T. Yao, Z. Sun, W. Cheng, S. He, Y. Xie, Y. Peng, H. Cheng, Y. Sun, Y. Jiang, F. Hu, Z. Xie, W. Yan, Z. Pan, Z. Wu and S. Wei, Nature Communications, 2014, 5, 5122.

288. J. Brillet, J. H. Yum, M. Cornuz, T. Hisatomi, R. Solarska, J. Augustynski, M. Gratzel and K. Sivula, Nature Photonics, 2012, 6, 824.

289. M. D. Symes and L. Cronin, Nature Chemistry, 2013, 5, 403.